Published in final edited form as:
Nat Neurosci. 2022 April ; 25(4): 458–473. doi:10.1038/s41593-022-01043-3.

Impaired neurogenesis alters brain biomechanics in a neuroprogenitor-based genetic subtype of congenital hydrocephalus

A full list of authors and affiliations appears at the end of the article.

Abstract

Hydrocephalus, characterized by cerebral ventricular dilatation, is routinely attributed to primary defects in cerebrospinal fluid (CSF) homeostasis. This fosters CSF shunting as the leading reason for brain surgery in children despite considerable disease heterogeneity. In this study, by integrating human brain transcriptomics with whole-exome sequencing of 483 patients with congenital hydrocephalus (CH), we found convergence of CH risk genes in embryonic neuroepithelial stem cells. Of all CH risk genes, *TRIM71/lin-41* harbors the most de novo mutations and is most specifically expressed in neuroepithelial cells. Mice harboring neuroepithelial cell-specific *Trim71* deletion or CH-specific *Trim71* mutation exhibit prenatal hydrocephalus. CH mutations disrupt TRIM71 binding to its RNA targets, causing premature neuroepithelial cell differentiation and reduced neurogenesis. Cortical hypoplasia leads to a

---

Reprints and permissions information is available at www.nature.com/reprints.

Correspondence and requests for materials should be addressed to Kristopher T. Kahle. kahle.kristopher@mgh.harvard.edu.

Author contributions
Conceptualization of the project: P.Q.D., S.C.W., W.K. and K.T.K. Data collection: P.Q.D., S.C.W., C.M., X.L., D.L., P.J.D., S.M., A.S., W.D., J.J., E.K., A.J.K., S.K., M.Z.P., L.A.T.-F., K.H., E.D.D., M.B., T.U., S.A.J., E.C., L.T.H., B.J., A.M.M.S., F.L., S.-K.K., M.L., Y.Y., Y.T., A. Duque, C.N.-W., Y.H., K.S., S.M.R., A.K.S., G.A., C.G.F., A.T.T., B.C.R., H.S., A. Dunbar, T.D., J.G., A.M., A.M.-D.-L., X.Y., W.E.B., B.S.C., E.M.R.L., R.T.C., P.R., H.L., E.D., H.B., N.M., J.I.E.-V., C.A.W., S.L.A., J.S., K.P., A. Doetzlhofer, F.G.W., S.C.J., R.P.L., N.S., W.K. and K.T.K. Data analysis: P.Q.D., S.C.W., C.M., X.L., D.L., P.J.D., S.M., A.S., W.D., J.J., E.K., A.J.K., S.K., M.Z.P., L.A.T.-F., K.H., E.D.D., M.B., T.U., S.A.J., E.C., L.T.H., B.J., A.M.M.S., F.L., S.-K.K., M.L., Y.Y., Y.T., A. Duque, C.N.-W., Y.H., K.S., S.M.R., A.K.S., G.A., C.G.F., A.T.T., B.C.R., H.S., A. Dunbar, T.D., J.G., A.M., A.M.-D.-L., X.Y., W.E.B., B.S.C., E.M.R.L., R.T.C., P.R., H.L., E.D., H.B., N.M., J.I.E.-V., C.A.W., S.L.A., J.S., K.P., A. Doetzlhofer, F.G.W., S.C.J., R.P.L., N.S., W.K. and K.T.K. Writing: P.Q.D., S.C.W., W.K. and K.T.K., with input from all authors.

Online content
Any methods, additional references, Nature Research reporting summaries, source data, extended data, supplementary information, acknowledgements, peer review information; details of author contributions and competing interests; and statements of data and code availability are available at https://doi.org/10.1038/s41593-022-01043-3.

Reporting Summary.
Further information on research design is available in the Nature Research Reporting Summary linked to this article.

Resource availability
All unique animal lines and cell lines in this study are available upon reasonable request to the corresponding author. Source data are provided with this paper.

Code availability
All code used in this paper is available from the corresponding author upon reasonable request.

Competing interests
J.J. is an employee of GeneDx, Inc.

Additional information
Extended data is available for this paper at https://doi.org/10.1038/s41593-022-01043-3.

Supplementary information The online version contains supplementary material available at https://doi.org/10.1038/s41593-022-01043-3.

Peer review information *Nature Neuroscience* thanks the anonymous reviewers for their contribution to the peer review of this work.

hypercompliant cortex and secondary ventricular enlargement without primary defects in CSF circulation. These data highlight the importance of precisely regulated neuroepithelial cell fate for normal brain–CSF biomechanics and support a clinically relevant neuroprogenitor-based paradigm of CH.

First described by Aristotle as a 'hollow' in the brain[1], the cerebral ventricles are CSF-filled cavities with increasingly recognized importance in cerebral development[2]. Enlargement of the cerebral ventricles characterizes hydrocephalus ('water on the brain'), which can present at any age. Infantile hydrocephalus, affecting 1/1,000 live births, is the leading reason for brain surgery in children and is associated with marked neurodevelopmental disability[3,4]. Hydrocephalus is classically attributed to impaired CSF circulation owing to defective cilia-driven flow currents or imbalance in fluid production and absorption, leading to intraventricular fluid overaccumulation that warrants neurosurgical shunting to reduce CSF volume as a default treatment[5]. Although CSF diversion can be acutely lifesaving, the persistence of poor neurodevelopmental outcomes in some patients despite shunting highlights the incomplete understanding of the disease[3]. To that end, whole-exome sequencing (WES) has identified mutations in regulators of prenatal neurogenesis as novel genetic causes of human idiopathic CH[6,7], suggesting that, in some instances, hydrocephalus may arise not from a primary CSF overaccumulation but, rather, from aberrant neurodevelopment. However, the mechanisms linking CH gene mutations to hydrocephalus remain poorly understood owing to the genetic heterogeneity of the disease, with more than 100 genetic loci implicating seemingly disparate biological processes[8]. Furthermore, mechanistic investigations are hindered by poor knowledge of when, where and what cell types in the brain are affected by a given gene mutation. Moreover, there is a lack of animal models harboring patient-specific human mutations.

In this study, we took a multi-pronged approach that coupled agnostic human functional genomics with hypothesis-driven experimental biology in mouse and stem cell models to define the mechanism of a human CH genetic subtype. By mapping the expression of CH risk genes defined by WES of human patients to large-scale gene expression atlases of typically developing human brains, we found that a heterogenous collection of ~100 CH risk genes converged in human neuroepithelial cells, which are neural stem cells that line the embryonic cerebral ventricles. To test the hypothesis that dysregulated neuroepithelial cell development is the primary pathology driving hydrocephalus, we focused our functional investigations on *TRIM71/lin-41*, which harbors the most de novo mutations (DNMs) and is most specifically expressed in embryonic neuroepithelial cells of all risk genes. Using the first humanized mouse model of hydrocephalus harboring a patient-specific missense mutation, we show that mutant TRIM71 polypeptide causes CH through molecular perturbations in neural stem cells that compromise cortical neurogenesis and associated parenchymal–CSF biomechanics in the absence of primary defects in CSF flow. These findings shift the paradigm of CH from a primary defect of CSF 'plumbing' to that of an inborn brain defect with secondarily enlarged ventricles arising from the defective temporal progression of neuroepithelial stem cells during the period of neural tube formation and early cortical neurogenesis.

Results

CH genetic risk converges in human neuroepithelial cells.

To understand the molecular genetic mechanisms of human CH, we coupled unbiased gene discovery in human patients with hypothesis-driven modeling of CH genes in model systems that permit functional insights into mechanisms by which mutant gene products cause disease[2]. We began by analyzing WES data of 1,061 individuals comprising 483 sporadic CH probands who have undergone surgery for therapeutic CSF diversion by a neurosurgeon (289 parent–offspring trios and 194 singletons; Methods and Supplementary Table 1). To our knowledge, this group constitutes the largest to-date international cohort of neurosurgically treated patients with CH to have undergone exome sequencing.

We identified 93 CH-associated risk genes from our WES data (defined as genes harboring at least one de novo protein-altering mutation with pLI ≥ 0.9 or mis-z ≥ 2) (Fig. 1a, Supplementary Table 2 and Methods). Analysis using PCNet (a resource of molecular interactions among human genes)[9,10] showed that CH risk genes exhibit a higher degree of interconnectivity to each other than expected by chance (Fig. 1b), suggesting functional coordination. Gene Ontology (GO) annotation of CH risk genes revealed enrichment in multiple nervous-system-related GO terms, including ‘nervous system development’, ‘synapse organization’ and ‘neuron projection development’ (Fig. 1c). Selected GO terms related to CSF homeostasis (for example, ‘cilium movement’, ‘cerebrospinal fluid circulation’ and ‘body fluid secretion’) were not enriched (Fig. 1c), in contrast to the classical dogma that implicates dysregulated CSF flow as the primary pathogenic process leading to ventricular expansion in hydrocephalus[5,8]. These data suggest convergence of ~100 apparently heterogeneous CH risk genes onto a limited number of biological processes affecting human brain development.

We next performed functional integrative genomic analyses combining our WES data with large-scale transcriptomic atlases of the human brain[11–14] to map when, where and in which cell types mutations in CH risk genes may exert their pathogenic effects to cause disease (Fig. 1a and Methods). We restricted input genes to the aforementioned 93 CH risk genes defined only by hypothesis-free exome sequencing in our study, minimizing biases associated with inputs that may have been identified in part based on their biological plausibility[15]. To evaluate spatiotemporal convergence among the 93 CH risk genes defined by WES, we leveraged published mRNA expression data generated by transcriptomic profiling (including bulk and single-cell RNA sequencing (scRNA-seq)) of normally developing human brains covering the entire lifespan of human development, from the first trimester of gestation to adulthood[11–14] (see Supplementary Table 3 for a summary all human datasets used). Analyzing the expression trajectories of disease-associated genes in typically developing human brain may provide insights into mechanisms dysregulated in hydrocephalus, thereby informing disease gene prioritization and the cellular contexts in which gene mutations might be most productively studied[15].

CH risk genes were diffusely expressed across all human prenatal cortical regions (Extended Data Fig. 1a) and statistically enriched from post-conception weeks (PCWs) 8–24 (Fig. 1d and Extended Data Fig. 1b), periods characterized by neuroprogenitor proliferation and neurogenesis[16]. Among different fetal human cortical layers, CH risk gene connectivity (defined by gene expression and PCNet molecular interactions; Methods) was enriched in the ventricular zone (VZ) and the inner subventricular zone (SVZi) (Fig. 1e and Extended Data Fig. 1c–e), which are germinal compartments lining the prenatal ventricular wall[16]. At the cell type level, CH risk gene expression was enriched in human prenatal excitatory neurons and neuroepithelial cells (Fig. 1f and Extended Data Fig. 1f), the earliest neural stem cells of the brain lining the embryonic ventricles[16]. Representative CH genes previously discovered by WES analysis (*TRIM71*, *PTEN*, *SMARCC1*, *FOXJ1* and *PIK3CA*)[7] and known familial CH genes (*L1CAM*, *AP1S2*, *MPDZ* and *CCDC88C*)[8] were expressed in neuroprogenitors (neuroepithelial cells, radial glia cells or intermediate progenitor cells) (Fig. 1g). In contrast, CH risk gene expression was not enriched in CSF system components based on analyses of other transcriptomic datasets[14,17,18], including ependymal cells (involved in local CSF flow), choroid plexus (involved in CSF production) or the arachnoid (involved in CSF reabsorption) (Extended Data Fig. 1g–i).

The convergence of CH risk gene expression in fetal cortical development suggests that CH may share developmental mechanisms with cortical malformations. We, thus, mapped various risk genes (CH, autism, schizophrenia, cerebral palsy, microcephaly, lissencephaly, polymicrogyria and primary ciliary dyskinesia (PCD)) onto molecular networks constructed by weighted gene co-expression network analysis (WGCNA) of human brain RNA sequencing data (Extended Data Fig. 2a, Supplementary Tables 2 and 4–11 and Methods). This approach organizes the human brain transcriptome into a smaller coherent set of gene co-expression networks or modules sharing distinct biological functions and co-regulatory relationships[19]. Testing each network for disease gene enrichment and functional annotation of the networks permits unbiased identification of disease-relevant biological processes[19].

Among the 87 WGCNA gene co-expression networks generated, CH risk genes were enriched in six networks (Fig. 1h and Extended Data Fig. 2b–g). Four of these networks were also enriched for other neurodevelopmental risk genes, suggesting overlap between CH and other malformations, such as microcephaly (Fig. 1h). The other two CH-enriched networks did not overlap with the other examined disorders. Despite the notion that motile ciliary dysfunction causes hydrocephalus[8], genes associated with CH and those causing the motile ciliary disorder PCD did not overlap in any common modules, suggesting that divergent biological processes underlie CH and PCD (Fig. 1h). Indeed, transcriptional connectivity between CH and cortical developmental disorder genes was stronger than that between CH and PCD genes (Extended Data Fig. 2h,i), linking CH etiology more to impaired cortical development rather than to dysfunction of motile cilia. GO annotation reveals that most of the shared molecular networks underlying CH and other cortical disorders enriched for broad molecular pathways regulating gene expression (such as ‘histone modification’ and ‘mRNA processing’), whereas networks specific for CH enriched for distinctly neurodevelopmental processes, including ‘primary neural tube formation’ (Fig. 1h and Extended Data Fig. 2b–g). Molecular networks, therefore, suggest shared etiologies between CH and cortical malformations defined by altered neurogenesis[20] and that the CH-relevant pathology may begin as early as the time of neurulation and early cortical neurogenesis.

A humanized *Trim71* mutant mouse model exhibits hydrocephalus.

Functional genomics revealed first trimester neuroepithelial stem cells as a spatiotemporal locus of disease gene convergence in the developing human brain and a promising cell type for further study of CH gene mutations. We, therefore, prioritized CH risk genes based not only on their mutation frequencies in our exome-sequenced cohort, but also on their expression levels in human neuroepithelial cells. *TRIM71/lin-41* was the most frequently de novo mutated CH risk gene in our studied patient cohort (Fig. 2a and Supplementary Table 12) and encodes an RNA-binding protein involved in stem cell fate determination[21]. Analysis of single-cell transcriptomic data of prenatal human brain[12] indicated that TRIM71 is the CH risk gene that is most specifically expressed in human neuroepithelial cells and in PCW5 brain (Fig. 2b). The mutation frequency in human patients and specific expression in a cell type of disease convergence focused the remainder of our study on *TRIM71* as a prototype gene in which to test the hypothesis that a subset of CH is driven primarily by genetically encoded dysregulation of neuroprogenitors.

TRIM71 harbored seven DNMs and one unphased mutation in eight unrelated CH probands, including a novel heterozygous de novo point mutation in the RNA-binding NHL domain of *TRIM71* (p.D624N; Fig. 2c). Among these are the recurrent heterozygous DNMs p.R608H and p.R796H located in conserved residues in analogous positions of TRIM71’s NHL domain (Fig. 2c). All *TRIM71*-mutant patients exhibited hydrocephalus at or soon after birth, with fetal ventriculomegaly apparent in most of those subjected to prenatal brain imaging (Fig. 2c,d).

The fetal onset of hydrocephalus in *TRIM71*-mutant patients prompted examination of the cellular composition of the cerebral ventricle wall in published bulk and single-cell transcriptomic data of prenatal human brain[13,14]. We analyzed expression of ependymal and neuroprogenitor cell markers in samples containing only VZ and SVZ (Fig. 2e–g). Neuroprogenitor markers *SOX2* and *PAX6* were expressed at significantly higher levels in PCW15–21 cerebral ventricle wall than was ependymal cell marker *FOXJ1* (Fig. 2f). Single-cell data revealed that PCW14–18.5 cerebral ventricle wall comprised predominantly of neurons and neuroprogenitors, whereas immature ependymal cells (defined as *FOXJ1*$^+$ radial glia cells) constituted only 0.56% of cells (4/717) (Fig. 2g). No mature ependymal cell (defined by markers from ref. [17]) was detected in PCW14–18.5 ventricle wall (Fig. 2g). Thus, at the time of fetal hydrocephalus diagnosis in *TRIM71*-mutant patients, the human ventricle wall is composed predominantly of neuroprogenitors and their neuronal descendants, consistent with previous histological studies demonstrating that multi-ciliated ependymal cells cover the ventricle wall only after birth in humans and mouse[22,23]. The fetal onset of hydrocephalus in *TRIM71*-mutant patients with CH before maturation of multi-ciliated ependyma suggests that loss of cilia-driven CSF flow cannot be the initiating cause of prenatal ventriculomegaly and further implicates neuroprogenitors in the developmental etiology of CH.

To validate *TRIM71* as a human CH gene and to gain mechanistic insight into CH-associated *TRIM71* mutations, we used CRISPR–Cas9 gene editing to generate *Trim71*^{R595H} mice harboring the murine homolog of the recurrent human CH-associated missense mutation p.R608H (Fig. 2c,h and Methods). Live brain MRI revealed severe ventriculomegaly detectable at birth (postnatal day (P) 0, the earliest time point examined) in ~16% of *Trim71*$^{R595H/+}$ mice (Fig. 2i), phenocopying the severe fetal hydrocephalus seen in *TRIM71*$^{R608H/+}$ human patients with CH (Fig. 2d). By P21, hydrocephalic *Trim71*$^{R595H/+}$ mice exhibited progressive ventriculomegaly (Fig. 2j) associated with macrocephaly and doming of the skull (Extended Data Fig. 3). Quantitative magnetic resonance imaging (MRI) analysis of brain anatomical development in P0 hydrocephalic *Trim71*$^{R595H/+}$ mice revealed ventriculomegaly with decreased cerebral cortex volume (cortical hypoplasia) despite normal intracranial volume (Fig. 2k–m). Intracranial volume at P21 was increased in hydrocephalic *Trim71*$^{R595H/+}$ mice, consistent with their gross macrocephaly (Fig. 2l and Extended Data Fig. 3). Thus, although hydrocephalic *Trim71*$^{R595H/+}$ mice do eventually exhibit progressive macrocephaly suggestive of intraventricular CSF accumulation, the primary anatomical defect at birth is cerebrocortical hypoplasia without calvarial ballooning.

Trim71 knockout (KO) mice exhibit embryonic lethality and failed rostral neural tube closure[24–27]. We found that homozygous *Trim71*$^{R595H/R595H}$ mutant mice exhibited completely penetrant exencephaly and embryonic lethality, as no homozygous mutant embryos could be recovered after apparent embryonic resorption by embryonic day (E) 13.5 (Fig. 2n–q). These severe defects in neural tube formation suggest that CH-associated mutations may perturb the earliest stages of cerebrocortical genesis to cause hydrocephalus.

Deletion of *Trim71* in neuroprogenitors causes hydrocephalus.

Analysis of published scRNA-seq data[12] reveals *TRIM71* expression almost exclusively in human brain neuroepithelial progenitors (Fig. 3a). *TRIM71* expression was evident at PCW5 (shortly after neurulation in humans) but undetectable by PCW6 and thereafter (Fig. 3b). *TRIM71* was minimally expressed in adult human cerebral cortex (Extended Data Fig. 4a). Examination of published mouse scRNA-seq data[28] revealed *Trim71* expression in neuroepithelial cells and at E9.5 (the time of neurulation in the mouse) (Fig. 3c,d). Analysis of an in vitro transcriptomic dataset of human induced pluripotent stem cells (iPSCs) undergoing neural differentiation[29] revealed the highest expression of *TRIM71* in undifferentiated iPSCs and at the earliest stages of neuroprogenitor progression, with a rapid decrease during the transition from neural rosette stage to neural differentiation (Fig. 3e). TRIM71 immunostaining in primary cells harvested from embryonic human neocortex[30] revealed robust TRIM71 expression in NES^{+} human neuroepithelial cells (Fig. 3f).

We next examined *Trim71* expression in mouse brain tissues to validate findings based on analyses of published transcriptomic datasets. RNAscope of E9.5 mouse neuroepithelium demonstrated robust *Trim71* expression, with downregulation by E12.5 (Fig. 3g–l). *Trim71* expression was absent from the postnatal multi-ciliated ependyma (Fig. 3i,l). Similarly, *Trim71* expression was detected in mouse embryonal carcinoma cells but not in *Foxj1*-expressing ependymal cell cultures (Extended Data Fig. 4b,c). Immunostaining revealed robust TRIM71 expression in E9.5 VIM^{+} neuroepithelial stem cells, followed by absence from E12.5 VZ and P7 ventricular ependyma (Fig. 3g–i,m–o). TRIM71 was not expressed in the postnatal mouse choroid plexus (Extended Data Fig. 4d). These results define TRIM71 as a novel marker of neuroepithelial cells lining the neural tube, with no functional expression in components of the CSF circulatory apparatus.

TRIM71 enrichment in embryonic neuroprogenitors prompted us to generate neuroprogenitor-specific *Trim71* KO mice by crossing either *Nestin:Cre* or *Emx1:Cre* to a conditional *Trim71* allele (Fig. 3p,q and Methods). Cre-mediated recombination deleted *Trim71* either in all neuroprogenitors (*Nestin-Trim71*$^{fl/fl}$)[31] or in a neuroprogenitor subset specified primarily for excitatory neurons of the forebrain neocortex (*Emx1-Trim71*$^{fl/-}$)[32]. *Trim71* conditional KO mice from either Cre drivers exhibited ventriculomegaly in a significant percentage of animals (~16% of *Nestin-Trim71*$^{fl/fl}$ mice and ~25% of *Emx1-Trim71*$^{fl/-}$ mice) (Fig. 3r,s and Extended Data Fig. 5a,b). To further define developmental periods at which TRIM71 is essential, we used a Tet-On conditional system in which doxycycline (dox) activates Cre protein expression driven by a ubiquitous promoter (Fig. 3t). *Trim71* KO at E5.5 resulted in completely penetrant neural tube defects at E12.5, whereas brain development appeared normal when *Trim71* was knocked out at P0.5 (immediately after birth; Fig. 3u,v). These results suggest that TRIM71 functions in embryonic development to regulate brain morphogenesis and implicate early forebrain neuroprogenitors as the key cell type relevant to hydrocephalus pathogenesis.

CH-associated *Trim71* mutation impairs cortical neurogenesis.

Motivated by previous studies demonstrating TRIM71 functions in stem cell fate[25,26,33] and by our systems biology analyses implicating neuroepithelial cells as a convergent target of ~100 CH risk genes (Fig. 1), we sought to examine the effect of CH-associated *TRIM71* mutations on neuroepithelial cell proliferation and differentiation. Using immunostaining, we found that E9.5 neuroepithelia of *Trim71*$^{R595H/+}$ and *Trim71*$^{R595H/R595H}$ embryos had fewer pH3$^+$ cells (cell proliferation marker) and more DCX$^+$ cells (marker of immature neurons) than wild-type (WT) embryos (Fig. 4a,b). *Trim71*$^{R595H/R595H}$ and *Trim71*$^{R595H/+}$ mouse embryonic stem cells (mESCs) were less proliferative than WT mESCs upon N2B27-induced neural differentiation, similar to *Trim71* KO mESCs (Fig. 4c,d and Extended Data Fig. 6a–c).

To investigate molecular changes caused by abnormal TRIM71 function, we performed RNA sequencing of the *Trim71*$^{R595H/R595H}$, *Trim71*$^{R595H/+}$, *Trim71* KO and their respective control mESCs, a cell type expressing high levels of TRIM71 (ref. [26]). Principal component analysis showed separation of *Trim71* KO and *Trim71*$^{R595H/R595H}$ from their respective control mESC lines in PC2, whereas *Trim71*$^{R595H/+}$ clustered with WT mESCs (Fig. 4e). CIBERSORT[34] analysis revealed a distinct shift in both *Trim71* KO and *Trim71*$^{R595H/R595H}$ mESCs toward neuroepithelial cell fates (Fig. 4f), indicating premature neural progression of the transcriptomes. Gene expression profiles across all five conditions could be clustered in ten different gene co-expression modules (Extended Data Fig. 6d and Supplementary Table 14). We focused on downregulated or upregulated genes in *Trim71* KO and *Trim71*$^{R595H/R595H}$ mESCs, which corresponded to the steelblue and gold modules, respectively. GO analysis of the corresponding genes showed enrichment in neurodevelopmental terms in both modules. Genes downregulated by mutant TRIM71 (steelblue) appeared in terms such as 'negative regulation of nervous system development/ neuron differentiation' (Fig. 4g,i), indicating a positive effect on neural development. Genes upregulated in *Trim71* KO and *Trim71*$^{R595H/R595H}$ mESCs (gold) appeared in 'neural tube development/formation' (Fig. 4h,j), also indicating a pro-neural development shift. We conclude that the CH-causing mutation R595H initiates precocious neural differentiation in the normally undifferentiated pluripotent stem cells, suggesting abnormally accelerated progression of stem cell state.

Premature neural differentiation in *Trim71* mutant mESCs suggests that impairments in stem cell progression may affect later cortical development. Motivated by our observation of perinatal cortical hypoplasia in hydrocephalic *Trim71*$^{R595H/+}$ mice, we examined cortical neurogenesis in the hydrocephalic *Trim71* mutant mouse models *Trim71*$^{R595H/+}$ and *Nestin-Trim71*$^{fl/fl}$. Immunostaining for markers of superficial (POUF32/BRN2) and deep (BCL11B/CTIP2 and TBR1) cortical layers revealed significantly reduced numbers of neurons in these layers in hydrocephalic *Trim71*$^{R595H/+}$ and *Nestin-Trim71*$^{fl/fl}$ mice at P0 as compared to their respective controls (Fig. 4k–p). The thicknesses of these layers were also reduced in hydrocephalic mice compared to controls (Fig. 4k–p). SVZ neural proliferation (based on immunostaining for the proliferation marker MKI67) was also significantly reduced in hydrocephalic *Trim71*$^{R595H/+}$ and *Nestin-Trim71*$^{fl/fl}$ mice compared to their respective controls (Fig. 4q–t). In contrast, apoptosis was minimal in neuroepithelia of WT, *Trim71*$^{R595H/+}$ and *Trim71*$^{R595H/R595H}$ E9.5 embryos (as in KO mice[25]) as well as in P0 brains of control and hydrocephalic *Trim71*$^{R595/+}$ and *Nestin-Trim71*$^{fl/fl}$ mice (Extended Data Fig. 7a–c). These results suggest that the thinned cerebral cortex in hydrocephalic *Trim71* mutant mice reflects impaired neurogenesis resulting from premature stem cell lineage commitment at the expense of neuroprogenitor proliferation.

Abnormal brain biomechanics facilitates ventriculomegaly.

To begin characterizing the physiologic mechanisms of hydrocephalus, we measured intracranial pressure and found it elevated at P7 in hydrocephalic *Trim71*$^{R595H/+}$ mice compared to WT controls (Fig. 5a), suggesting CSF overaccumulation. To investigate impaired CSF outflow as a potential cause of CSF overaccumulation, we developed an in vivo imaging strategy using the IVIS Lumina X5 animal imaging in neonatal mice, based on previous studies in adult animals (Fig. 5b and Methods)[35]. The Evans blue CSF tracer distributed to the cisterna magna and spinal cord 60 minutes after intraventricular injection in control mice (Fig. 5c), demonstrating the expected pattern of CSF outflow from the ventricles. In hydrocephalic *Trim71*$^{R595H/+}$ mice, reduced tracer distribution was observed in the cisterna magna and spinal cord, although tracer was clearly observed in the third ventricles on imaging of dissected brains (Fig. 5c–f). These findings demonstrate impaired CSF outflow from the forebrain ventricles in hydrocephalic *Trim71*$^{R595H/+}$ mice.

Aqueductal stenosis is the most common cause of impaired CSF outflow[5]. P0 hydrocephalic *Trim71* mutant mice (*Trim71*$^{R595H/+}$ and *Nestin-Trim71*$^{fl/fl}$) exhibited histological and (live) MRI patency of the midbrain cerebral aqueduct (Fig. 5g–i and Extended Data Fig. 8), but the aqueduct narrowed by P21 in the hydrocephalic *Trim71*$^{R595H/+}$ mice (Fig. 5j). Aqueductal stenosis also appeared to be a secondary phenomenon in a human *TRIM71* mutant patient with hydrocephalus, because the aqueduct re-expanded after CSF diversion surgery (Fig. 5k). In contrast, the aqueduct remained stenosed after CSF diversion in a hydrocephalic patient with a mutation in *L1CAM*, a classic aqueductal stenosis gene (Fig. 5k). Thus, although aqueductal stenosis may contribute to progressively worsening abnormalities in

CSF circulation, it is not causally related to the neonatal forebrain ventriculomegaly of *Trim71*$^{R595H/+}$ mice.

To examine other physiological causes of forebrain ventriculomegaly, we stained for markers of ependyma and choroid plexus and found that ependymal and choroid plexus cells appeared morphologically normal in P0 hydrocephalic *Trim71*$^{R595H/+}$ and *Nestin-Trim71*$^{fl/fl}$ mutant mice (Extended Data Fig. 9a). Molecular correlates of CSF hypersecretion (phospho-SLC12A2/NKCC1 and phospho-STK39/SPAK immunostaining)[36] were unaltered in hydrocephalic *Trim71*$^{R595H/+}$ mice (Extended Data Fig. 9b–d). We examined ependymal ciliary function with an optical coherence tomography (OCT) imaging approach previously used in *Xenopus*[37], visualizing ependymal flow by OCT imaging of polystyrene beads moving over freshly dissected coronal brain slices containing the lateral ventricles (Fig. 6a). Ex vivo ciliary beating by ependymal cells drives bead movement, reflecting CSF flow (Fig. 6a and Supplementary Movie). Ciliobrevin-mediated inhibition[38] of dynein, which powers the motile cilia beating, resulted in reduced ependymal flow that was partially restored by toxin washout (Extended Data Fig. 9e,f and Supplementary Movie). We characterized maturation of cilia-driven flow in the lateral ventricle during normal mouse development using this OCT system. We found that minimal flow was detected at birth (when hydrocephalus in *Trim71*$^{R595H/+}$ mice was already detected), and ependymal flow did not mature until P7 (Fig. 6b,c). Cilia-generated CSF flow was unaffected in P7 hydrocephalic *Trim71*$^{R595H/+}$ mice (Fig. 6d,e and Extended Data Fig. 9g–i). These data suggest that abnormal ependymal cilia are not required for initiation or progression of hydrocephalus in *Trim71*$^{R595H/+}$ mice.

The above results argue against defects in active CSF circulation as primary causes of forebrain ventriculomegaly in *Trim71*$^{R595H/+}$ mice. However, an often overlooked component in intracranial physiology is the cerebral parenchyma itself. Indeed, a positive pressure always exists inside the lumen of the ventricular system, because, otherwise, the overlying neural tube and brain parenchyma compartment (the ‘vessels’ holding the fluid) would collapse. This pressure generated by CSF in the lumen must be balanced by forces exerted by neural tissue surrounding the fluid to prevent ventricular expansion. The absence or reduction of such counteracting forces by neural tissue may potentially facilitate ventricular dilation and passive intraventricular CSF pooling[2,39,40].

To test the hypothesis that altered brain biomechanics facilitates ventricular dilation, we used atomic force microscopy (AFM)[41–43] to measure biomechanical properties of brain tissue in WT and hydrocephalic *Trim71*$^{R595H/+}$ mice. AFM allows direct force measurements from which tissue stiffness and the viscoelastic properties, creep compliance, and relaxation modulus can be calculated. These properties reflect the resilience of material under strain. AFM indentations on dissected brain tissues from WT and hydrocephalic *Trim71*$^{R595H/+}$ mice revealed a significant reduction in stiffness and relaxation modulus in P7 *Trim71*$^{R595H/+}$ hydrocephalic brain tissues compared to WT tissues, whereas mutant compliance was significantly increased (Fig. 6f–i). These alterations suggest that reduced cortical neurogenesis in hydrocephalic *Trim71*$^{R595H/+}$ mice renders the hypoplastic brains hypercompliant and less able to resist mechanical strain, leading to accommodation of greater CSF volume at any given CSF pressure. These changes facilitate secondary enlargement of the ventricles in the absence of aqueductal stenosis, but continued expansion of forebrain parenchyma can later compress the midbrain cerebral aqueduct located between the expanding cerebral hemispheres (Fig. 6j). Our observations highlight effects on brain–fluid biomechanics as physiological parameters that link impaired neurogenesis to secondary enlargement of ventricles underlying hydrocephalus in *Trim71*$^{R595H/+}$ mice.

CH-associated *TRIM71* mutations disrupt RNA binding.

Next, we investigated the molecular mechanisms that underlie the effect of *TRIM71* mutations, which clustered in the NHL domain (Fig. 7a). We confirmed normal distribution and stability of CH mutant TRIM71 protein by immunostaining in E9.5 neural tube as well as immunoblotting of mESC lysates (Fig. 7b,c). To investigate whether CH-associated mutations affect RING finger ubiquitination activity[25,27], we immunoprecipitated SHCBP1 from lysates of WT, *Trim71* KO, and *Trim71*$^{R595H/R595H}$ mESCs after neural induction with retinoic acid (RA). Immunoblots revealed two bands (Fig. 7d), the lower of which co-migrates with SHCBP1. The upper band overlapped with a distinct ubiquitin signal, and the mass increment of ~8.6 kDa matches that of the mono-ubiquitylation previously described for SHCBP1 (ref. [27]). Mono-ubiquitylated SHCBP1 was reduced in *Trim71* KO mESCs, whereas mono-ubiquitylated SHCBP1 in *Trim71*$^{R595H/R595H}$ mESCs remained unchanged (Fig. 6e). Thus, TRIM71 R595H mutation does not interfere with its E3 ubiquitin ligase activity.

The recurrent CH-causing *TRIM71* mutations R608H and R796H affect conserved residues in the NHL domain (indicated in Fig. 7a) that is essential for RNA binding[44], suggesting that these mutations may impair TRIM71 binding to RNA[6,7]. To test this hypothesis, we generated mESCs expressing endogenous levels of FLAG-tagged WT- or (CH-mutant) R595H-TRIM71 and performed photoactivatable-ribonucleoside-enhanced crosslinking and immunoprecipitation (PAR-CLIP) (Methods)[45] combined with gel electrophoresis and radiography. RNA co-precipitated with WT-TRIM71 and the DHX36 positive control, whereas RNA binding was severely depleted in TRIM71-R595H PAR-CLIP (Fig. 7f).

We next investigated whether CH mutant TRIM71 retains binding to known mRNA targets, including the cell cycle inhibitor *CDKN1A*[44] and the transcription factor *EGR1* (ref. [33]), which balance stem cell proliferation and differentiation[33,44,46]. We overexpressed FLAG-tagged, human TRIM71-WT, -CH-mutant (R608H and R796H) or −ΔNHL6 (RNA-binding deficient mutant)[24,44] in HEK293T cells and performed CLIP, followed by qRT–PCR. Both *CDKN1A* and *EGR1* were significantly reduced in TRIM71-R608 and −R796H as well as in TRIM71-ΔNHL6 (Fig. 7g,h and Extended Data Fig. 10a). Similarly, in CLIP-qRT–PCR with mESCs expressing endogenous levels of WT- or CH-mutant (R595H) TRIM71, binding of *Cdkn1a* and *Egr1* was enriched by WT and reduced by CH mutant TRIM71-R595H (Fig. 7i and Extended Data Fig. 10b). Correspondingly, *Cdkn1a* and *Egr1* RNA (Fig. 7j) and protein levels were dysregulated (Extended Data Fig. 10c–e) in CH mutant mESCs. Luciferase assays corroborated reduced repression of the *CDKN1A* 3′ untranslated region (UTR) by TRIM71-R608H, TRIM71-R796H, and TRIM71-ΔNHL6 in HEK293T cells and in *Trim71*$^{R595H/R595H}$ and *Trim71* KO mESCs (Extended Data Fig. 10f–i). CH-causing mutations also impaired TRIM71 binding to UPF1 (Extended Data Fig. 10j,k), a nonsense-mediated decay factor that cooperates with TRIM71 to repress mRNA targets[44]. These results demonstrate that CH mutations in TRIM71 impair degradation of RNA targets involved in regulating stem cell proliferation–differentiation balance[33,44,46].

Finally, we aimed to identify novel RNA targets of TRIM71 relevant to the neurodevelopmental etiology of CH. We used a stepwise approach to predict and functionally validate novel TRIM71 targets (summarized by Fig. 7k). We compiled from scRNA-seq data of the prenatal human cortex[12] a list of 100 genes that correlate or anti-correlate with *TRIM71* expression (Fig. 7k and Supplementary Tables 15 and 16). Consistent with TRIM71's role in promoting differentiation, genes anti-correlated with *TRIM71* expression were enriched for GO terms related to neurogenesis and in differentiated neurons (Fig. 7k). As TRIM71 represses RNA targets[44], we reasoned that genes anti-correlated with *TRIM71* expression likely represent potential TRIM71 RNA targets. Nineteen of these genes harbored at least one rare damaging mutation in our sequenced CH patient cohort (Methods and Supplementary Table 17). We ranked these genes according to TRIM71 binding as predicted by a published TRIM71 CLIP-seq dataset[47] and tested the top six putative targets (Fig. 7k).

By qPCR, three of these putative targets (*Inhbb*, *Cbfa2t2,* and *Spred1*) were de-repressed in *Trim71* KO and *Trim71*$^{R595H/R595H}$ mESCs and, in the case of *Spred1*, also in *Trim71*$^{R595H/+}$ mESCs (Fig. 7l). By CLIP–qPCR, *Inhbb*, *Cbfa2t2,* and *Spred1* were enriched in WT-TRIM71 CLIP over control but reduced in the TRIM71-R595H CLIP, suggesting impaired TRIM71 binding to these RNA targets (Fig. 7m). Intriguingly, *Spred1* overexpression has been shown to promote neural differentiation in the embryonic cortex[48], similar to the accelerated differentiation observed in *Trim71* mutant mESCs and mouse models. We, thus, identified three novel TRIM71 targets also mutated in our human CH cohort. Impaired TRIM71 regulation of these targets likely provides the molecular link between CH-associated TRIM71 mutations and premature stem cell progression, leading to impaired neurogenesis and altered brain–fluid biomechanics responsible for ventricular dilation.

Discussion

Hydrocephalus is classically attributed to deranged CSF flow, warranting neurosurgical CSF diversion as the primary treatment strategy despite minimal benefit in subsets of patients or, worse still, morbidity due to shunt infection or complications. Here we show that altered neural stem cell fate drives ventricular and brain malformations in a monogenetic subtype of hydrocephalus without primary defects in CSF circulation (overall findings summarized in Fig. 8).

We first mapped ~100 CH risk genes to human embryonic ventricular neuroepithelial cells, in which *TRIM71* is the most specifically expressed CH gene that also harbors the most DNMs. Patient-associated missense mutations in *TRIM71* disrupt TRIM71 binding to its RNA targets, resulting in premature stem cell differentiation that sets up deficient neuroprogenitor proliferation, leading to exencephaly (*Trim71*$^{R595H/R595H}$) or prenatal hydrocephalus with reduced cerebrocortical neurogenesis (*Trim71*$^{R595H/+}$). These phenotypes were recapitulated by forebrain neuroprogenitor-specific deletion of *Trim71* (causing hydrocephalus) or conditional KO of *Trim71* at E5.5 (causing exencephaly), supporting the hypothesis that the relevant pathology occurs in forebrain neuroepithelial cells around the time of neurulation and early cortical neurogenesis. Impaired neurogenesis renders a floppy cerebrocortical wall with reduced stiffness and hypercompliance, facilitating passive pooling of CSF and secondary distention of the ventricles despite unaffected cilia-generated CSF flow. We, thus, highlight the importance of precisely regulated neuroepithelial cell fate and neurogenesis for maintaining normal brain–CSF biomechanical interactions that limit ventricular expansion. Although the focus is on CH, we demonstrate that some, or potentially many, forms of CH are, in fact, a congenital brain malformation akin to microcephaly with secondarily enlarged ventricles rather than a primary disturbance in CSF circulation. Indeed, our data highlighting neural tube neuroepithelial cells as the spatiotemporal locus of disease pathogenesis support that idiopathic hydrocephalus should perhaps be considered part of the spectrum of neural tube defects[8].

The mechanisms outlined by our work are likely also relevant for other forms of CH beyond *TRIM71*, because our functional investigations were informed by unbiased functional genomic analyses of ~100 heterogeneous CH risk genes convergent on neuroepithelial cells. Although other CH gene mutations may exert molecular effects distinct from those of *TRIM71*, such as neuroprogenitor hyperproliferation in the case of *PTEN* mutations[49], these heterogenous molecular mechanisms may nonetheless converge in a predisposition to cortical dysgenesis that facilitates secondary ventricular enlargement. A more nuanced framework of hydrocephalus pathophysiology and CSF circulation should, thus, consider not only CSF components within the ventricular lumen but also how this fluid interacts with the surrounding brain parenchymal tissue. Given that the pressure within the ventricles is always a positive value because, otherwise, the brain would collapse, counteracting forces provided by the brain parenchyma are necessary to resist intraventricular CSF pressure to limit ventricular expansion[2,39]. Factors that lead to altered brain biomechanical properties, such as defective neurogenesis, could impair the ability of brain tissue to hold the pressure exerted by CSF and, thus, facilitate ventricular expansion as demonstrated in *TRIM71*-mutant CH. Future explorations of brain–CSF biomechanics in other genetic and acquired forms of infantile hydrocephalus will be essential for advancing knowledge of hydrocephalus pathogenesis and how brain biomechanics and anatomy influence the efficiency of CSF pulsation and movement[40].

The argument for neurogenic defects as the cause of CH raises an intriguing question: what explains the differences between hydrocephalus and microcephaly, a disorder of impaired neurogenesis typically unaccompanied by the macrocephaly characteristic of hydrocephalus? We contend that hydrocephalus and microcephaly are not mutually exclusive. First, longitudinal neuroimaging of human patients has shown examples of predominantly microcephalic phenotype (small head circumference and small cortex) that later progress to clinically significant ‘classic’ hydrocephalus marked by ventriculomegaly and rapidly increasing head circumference with signs of elevated intracranial pressure[50]. Thus, hydrocephalus can arise as a complication of a microcephaly phenotype. Second, microcephaly and CH exhibit genetic overlap. *WDR81* mutations can cause both prototypical CH (ventriculomegaly and macrocephaly)[51] and prototypical microcephaly (small cortex and low head circumference)[52]. In both situations (hydrocephalus versus microcephaly), a thin/small cerebral cortex is the overlapping structural brain anomaly. These observations suggest greater biological overlap than previously appreciated between microcephaly and hydrocephalus, perhaps explained by a convergent cellular pathology underlying cortical hypoplasia in both disorders. This hypothesis is supported by our computational analyses showing the convergence of CH and microcephaly risk genes in the same transcriptional networks of the developing human brain.

The mechanistic insights from our work provide explanatory power and translational value for the clinical care of patients with hydrocephalus. First, the finding that ventriculomegaly was already detectable by non-invasive fetal imaging in most *TRIM71*-mutant patients with hydrocephalus suggests that fetal ventricular enlargement is a relevant feature of CH. Prenatal imaging may, thus, be useful for clinical decision-making. Second, the demonstration of acquired aqueductal stenosis from an anatomically non-obstructive phenotype highlights the possibility that the biomechanical defects may progress due to mechanical stresses, warranting prospective monitoring even when a molecular diagnosis suggests a primary neurogenic deficit. To that end, brain stiffness and viscoelasticity may emerge as clinically relevant biomarkers for plotting timing and modality of surgical interventions in specific patients[39]. Third, our work highlights the need to expand the range of therapeutic options beyond neurosurgical CSF diversion to include approaches that optimize neurodevelopment, including behavioral intervention programs directed at improving cognitive and neurobehavioral function, starting from the time of diagnosis. Exome sequencing as a diagnostic adjunct may have utility in this regard[53]. In the long term, the definitive cure may require in utero personalized gene therapy or pharmacological approaches to correct the neurodevelopmental pathology of CH.

Our finding of abnormal neural stem cell fate driving ventricular malformation in CH suggests that similar mechanisms affecting cortical progenitors may also explain frequent observations of ventricular dysmorphology and neuropsychiatric dysfunction in other pediatric brain disorders, such as autism[2]. In fact, cerebrocortical neurons are not generated locally in the gray matter but, instead, originate from neuroprogenitors that line the developing ventricles[16,54]. Thus, crucial steps of cortical neurogenesis and differentiation occur at the brain–CSF interface populated by neural stem cells, underscoring the importance of precise neuroprogenitor regulation for maintaining brain–CSF biomechanical interactions in brain development. The mechanisms at play in hydrocephalus and TRIM71 functions may apply more broadly than previously appreciated to the understanding of human cerebrocortical development and disease[2].

Methods

We confirm that our research complies with all relevant ethical regulations as approved by the Yale University Human Investigation Committee, the Yale University Institutional Animal Care and Use Committee, the Johns Hopkins University School of Medicine Institutional Animal Care and Use Committee, the Berlin Landesamt für Gesundheit und Soziales, and the animal welfare committee of the Charité, Berlin.

Statistics and reproducibility.

No statistical method was used to predetermine sample size, but our sample sizes are similar to those reported in previous publications[25,26]. No data were excluded from the analyses. Randomization was not relevant to this study as controls and mutant mouse lines did not receive different treatments; human studies were descriptive studies; and cell line experiments were generated using the same experimental conditions. All experiments were performed and analyzed in a blinded manner. All experiments described have been replicated independently with similar results at least three times or in at least two independent cohorts of animals (including representative experiments shown in Figs. 2n–q, 3f,j–o, 4a, 5g and 7b,c and Extended Data Figs. 4b–d, 7a–c, 8 and 9a–d). Data distribution was assumed to be normal, but this was not formally tested.

Patients with CH.

The study protocol was approved by the Yale Human Investigation Committee. Written informed consent for genetic studies was obtained from all participants. Parent or legal guardian authorization was obtained in writing for sample collection of all minors in this study. Participants were not compensated for their participation. Inclusion criteria included patients with primary CH who did not carry a genetic diagnosis before surgical treatment or inclusion in the study. Patients with either a known chromosomal aneuploidy or a copy number variation with known association to CH were excluded. Hydrocephalus cases with secondarily acquired etiologies, such as intraventricular hemorrhage, meningitis, obstruction due to tumors or cysts and stroke, were excluded. Children with hydranencephaly, large cysts and cephaloceles, obvious posterior fossa crowding, myelomeningocele (Chiari II syndrome) or benign extra-axial CSF accumulation (that is, benign external hydrocephalus) were also excluded. Sequenced trios were composed of 483 primary CH probands, including 289 parent–offspring trios and 194 singletons. All probands had undergone surgery for therapeutic CSF diversion (shunt placement and/or endoscopic third ventriculostomy) and did not carry a genetic or clinical diagnosis of a known syndrome at the time of study recruitment. Patients and participating family members provided buccal swab samples (Isohelix SK-2S DNA buccal swab kits), medical records, neuroimaging studies, operative reports and CH phenotype data. Available demographic data of participants are included in Supplementary Table 1.

Exome sequencing and analysis.

Exon capture was performed using Roche SeqCap EZ MedExome Target Enrichment Kit or IDT xGen target capture kit, followed by paired-end sequencing on the Illumina platforms, as described previously[6,55]. Sequence reads were aligned to the human reference genome GRCh37/hg19 using BWA-MEM. Single-nucleotide variants and small indels were called using a combination of GATK HaplotypeCaller[56,57] and FreeBayes[58]. Allele frequencies were annotated in the Exome Aggregation Consortium, gnomAD and BRAVO databases[59–61]. MetaSVM and MPC algorithms were used to predict deleteriousness of missense variants (‘D-mis’, defined as MetaSVM-deleterious or MPC score ≥2)[62,63]. Inferred loss-of-function (LoF) variants consist of stop-gain, stop-loss, frameshift insertions/

deletions, canonical splice site and start-loss. LoF and D-mis mutations were considered ‘damaging’. PCR amplicons containing the mutation verified mutations in genes of interest.

DNMs were called using TrioDeNovo[64] and filtered as previously described[65]. After filtering using the aforementioned criteria, in silico visualization using Integrative Genomics Viewer was performed to remove false-positive calls[66]. Variants were confirmed by Sanger sequencing.

Kinship analysis.

The relationship between proband and parents was estimated using the pairwise identity-by-descent (IBD) calculation in PLINK. The IBD sharing between the proband and parents in all trios is between 45% and 55%. To further confirm that one proband was not biologically related to another, control cohorts or both, we calculated the overlap of high-confidence rare variants between each pair of individuals. For pairs that share ≥80% of rare variants, the sample with greater sequence coverage was kept in the analysis, and the other was discarded[65].

Principal component analysis.

To determine the ethnicity of each patient, we used the EIGENSTRAT software[67] to analyze tag single-nucleotide polymorphisms in cases, controls and HapMap samples, as previously described[65].

Gene-level DNM enrichment analysis.

The R package denovolyzeR was used for the analysis of DNMs based on a mutation model developed previously[68]. *P* values were calculated using a one-tailed Poisson test comparing the observed number of DNMs for each gene versus expected. As separate tests were performed for protein-altering, protein-damaging and LoF DNMs, the Bonferroni multiple testing threshold is equal to 8.6×10^{-7} (= 0.05 / (3 tests × 19,347 genes)). The most significant *P* value of the three tests was reported.

Curation of risk gene lists.

Risk genes from our CH cohort were defined as genes with pLI > 0.9 (intolerant to LoF mutations) or mis-Z > 2 (intolerant to missense mutations) that harbor at least one de novo protein-altering mutation (Supplementary Dataset 1). Risk genes for cerebral palsy were compiled from a previous exome sequencing study of human patients with cerebral palsy[69] (Supplementary Table 5). Risk genes for autism (Supplementary Table 4), schizophrenia (Supplementary Table 6), microcephaly (Supplementary Table 7), lissencephaly (Supplementary Table 8), polymicrogyria (Supplementary Table 9) and primary ciliary dyskinesia (Supplementary Dataset 10) were extracted from DisGeNET (https://www.disgenet.org)[70].

Expression of CH risk genes in PsychENCODE bulk RNA sequencing.

To summarize the expression pattern of CH risk genes along human brain development, we extracted the RPKM expression of these genes from the PsychENCODE bulk tissue RNA sequencing dataset[12]. We then scaled and centered the gene expression and calculated the average values for each gene across developmental periods. The expression distributions of all genes were visualized in a box plot, and the significance of expression enrichment was tested by comparing each development period to all other periods using one-tailed Wilcoxon rank-sum test.

PCNet risk gene interconnectivity analysis.

We performed the permutation tests to detect that whether the interconnectivity of CH risk genes in PCNet is higher than expected by chance, as previously published[10]. In brief, we downloaded the connected gene pairs in PCNet-V1.3 (ref. [9]) via https://bitbucket.org/willseylab/ (PCNet-V1.3_interactions.txt)[10]. Then, we measured three different kinds of interconnectivity as previously: (1) total number of pairwise connections among CH risk genes; (2) total number of CH risk genes connected to another CH risk gene (unique genes from A); and (3) number of direct connections between CH risk genes and any other PCNet genes. We permuted CH risk genes by randomly selecting the same number of connected gene pairs from PCNet. We permuted CH risk genes for 1,000 times and calculated above three kinds of interconnectivity. We estimated the significance of the CH risk gene interconnectivity by calculating the number of times out of 1,000 that we observed a permuted value greater than the observed value.

BrainSpan layer-specific risk gene network connectivity analysis.

We downloaded the processed BrainSpan layer-specific data (BrainSpan-Data_byLayer_cleaned.RData) via https://bitbucket.org/willseylab/ (ref. [10]). These data include BrainSpan frontal neocortex samples from PCW15 and PCW16 donors with seven layers: outer cortical plate (CPo), inner cortical plate (CPi), subplate zone (SZ), intermediate zone (IZ), outer subventricular zone (SZo), inner subventricular zone (SZi) and ventricular zone (VZ). First, we kept only the expressed hydrocephalus risk genes in each layer. To identify network connectivity in each layer, we calculated the average absolute values of Spearman’s correlation between connected hydrocephalus risk genes in PCNet, using expression data from each layer. Then, we normalized correlation by dividing the average absolute values of Spearman’s correlation for all gene pairs from CH risk genes for each layer, which is the network connectivity (per interaction). Finally, we permuted CH risk genes for 1,000 times by randomly selecting the same number of connected gene pairs from PCNet and calculated the network connectivity (per interaction). We estimated the significance of the CH risk gene network connectivity (per interaction) by calculating the number of times out of 1,000 that we observed a permuted value greater than the observed value.

Cell type enrichment of CH risk genes.

Cell type enrichment for the expression of CH risk genes was tested in prenatal human brain[12,14], postnatal mouse V-SVZ[17] and prenatal mouse meninges[18] in scRNA-seq datasets using in-house custom-made script in R studio. Enrichment for each cell type was tested using hypergeometric test. A gene list is considered to be significantly enriched in a cell type if the adjusted P value was less than 0.05. Average expression of CH risk genes in each cell type was shown using the DotPlot function from the Seurat package.

Co-expression network of CH and other developmental disorder risk genes.

Co-expression of custom annotated developmental disorder risk genes were first calculated using PsychENCODE bulk tissue RNA sequencing data[12], and a threshold of 0.65 was adopted to remove weak connections. Then, all the connected nodes, together with all primary ciliary dyskinesia genes, were used to build the network using multi-dimensional scaling layout algorithm. With this threshold, we calculated the percentage of risk genes from a given developmental disorder that each CH risk gene connected with, termed as connectivity. The distributions of the connectivity was visualized in a violin plot.

WGCNA.

A processed bulk mRNA sequencing expression dataset encompassing 16 human brain regions across human development[12] was used for robust consensus WGCNA (rWGCNA). The analysis was limited to the time points between PCW9 and postnatal year 3. Samples that are more than 3 standard deviations above the mean sample network connectivity were removed. Network analysis was performed with rWGCNA[71] assigning genes to specific modules based on bi-weight mid-correlations among genes. Soft threshold power of 10 was chosen to achieve scale-free topology ($r^2 > 0.9$). Then, a signed co-expression network was generated. The topological overlap matrix was clustered hierarchically using average linkage hierarchical clustering (using '1 – TOM' as a dis-similarity measure). The topological overlap dendrogram was used to define modules using minimum module size of 40, deep split of 4 and merge threshold of 0.1.

Module enrichment analysis.

Module gene lists were obtained via WGCNA as described above. In a background set of all genes categorized in co-expression modules, logistic regression was used for an indicator-based enrichment: is.disease ~ is.module + gene covariates (GC content, gene length and mean expression in bulk RNA sequencing atlas), as described previously[72]. Of the 88 WGCNA modules, the gray module contains all genes that do not co-express and are consequently unassigned to a co-expression network. Thus, the gray module was excluded from enrichment testing, and enrichment significance was defined at the Bonferroni multiple testing cutoff ($\alpha = 5.68 \times 10^{-4}$).

Animals.

All experiments using mice were performed in accordance with protocols approved by the Institutional Animal Care and Use Committees of Yale University and Johns Hopkins University School of Medicine, the Berlin Landesamt für Gesundheit und Soziales, and the animal welfare committee of the Charité, Berlin. Mice were reared in group housing of fewer than five mice per cage at 25 °C and 56% humidity on a 12-hour light/dark cycle and provided food and water ad libitum, with veterinary care provided by the Yale Animal Resource Center. Mice were maintained on the C57BL/6J background, and both sexes were used. See Supplementary Table 13 for the number of mice used for each experiment.

Trim71^{R595H} mutant mice were generated as described below. *Nestin-cre* (Jackson Laboratory, 003771) mice were mated with *Trim71*$^{fl/fl}$ mice[26] to obtain *Nestin-Trim71*$^{fl/fl}$ mice in which Trim71 is conditionally deleted from embryonic NSCs. *Emx1-Cre* (Jackson

Laboratory, 005628) were mated with a novel Cre-dependent *Trim71* allele (Fig. 3q) to obtain *Emx1-Trim71*$^{fl/–}$ in which Trim71 is conditionally deleted from embryonic NSCs. *TetO-cre* (006234) *and R26*^{rtTA*M2} (006965) mice were purchased from Jackson Laboratory. We crossed *TetO-cre tg*;*Trim71*$^{fl/fl}$ males/females with *Trim71*$^{fl/fl}$; *R26*$^{rtTA*M2/rtTA*M2}$ males/females to obtain *Trim71* KO (*TetO-cre tg*; *R26*$^{rtTA*M2/+}$; *Trim71*$^{fl/fl}$) and control littermates (*R26*$^{rtTA*M2/+}$;*Trim71*$^{fl/fl}$). To induce Cre expression, dox was delivered to time-mated females via ad libitum access to feed containing 2 g kg$^{−1}$ of dox.

CRISPR–Cas9 generation of *Trim71* R595H mutant mice.

Trim71 R595H mice were generated by the Yale Genome Editing Center. Mutation of TRIM71 R595 (human homolog, R608) to a histidine codon (AGG→CAT) was performed via CRISPR–Cas-mediated genome editing essentially as previously described[73,74]. Potential Cas9 target guide (protospacer) sequences in the vicinity of the R595 AGG codon were screened using the online tool CRISPOR (http://crispor.tefor.net).

Templates for single guide RNA (sgRNA) synthesis were generated by PCR, and sgRNAs were transcribed in vitro and purified using MEGAshortscript and MEGAclear kits (Life Technologies). Cas9 (enzyme) was purchased from New England Biolabs. Candidate sgRNA/Cas9 ribonucleoproteins (RNPs) were complexed and tested by zygote electroporation, incubation of embryos to blastocyst stage and genotype scoring by indel creation at the target site. The sgRNA containing the protospacer sequence CGGCAGTGAAGGTGACGGGG was highly efficient and was used for mouse creation.

sgRNA/Cas9 RNP was co-electroporated with a 127-base pair (bp) repair oligonucleotide into C57Bl/6J zygotes. The asymmetric repair oligo (‘reverse strand’) incorporates the reverse complement of the codon substituting R^{595} to H and three additional base mutations to prevent re-editing of the newly created allele. The repair oligo sequence 5′-ACCTGGATTCTGTTATTGCTTCGGTCAGCCACTATGATGAAACCCTCCTTATCAAC ACTCACGCCCCAGGGATGGCAGAGCTTGCCTTCACCATCACCTTCACTGCCGAAG CTCAGCCCGGGGAGCC was synthesized by IDT. Electroporated zygotes were transferred to pseudo-pregnant CD-1 foster females using standard techniques[75]. Genotyping was performed by PCR amplification followed by Sanger sequencing a 421-bp fragment. Primers for PCR are TrimF 5′-GACGGAAACCTGTTTGGTGC and TrimR 5′-GTCGGCCACTATGATCCTGC. Correct alleles were confirmed by TA cloning of PCR products and sequencing. Five mice carrying the proper mutation were identified and crossed to C57BL/6J mice to demonstrate germline transmission. The lines were then further back-crossed to breed out any off-target mutations.

Generation of *Trim71*^{R595H} and *Trim71* KO mESC lines.

R595H heterozygous female mice were super-ovulated and mated with R595H heterozygous males. Blastocyst stage embryos were collected and cultured using 2i + LIF as previously described[76]. Colonies that exhibited embryonic stem morphology were expanded and genotyped, and *Trim71*$^{R595H/+}$, *Trim71*$^{R595H/R595H}$ and *Trim71*$^{+/+}$ clones were used for subsequent experiments. *Trim71* KO mESCs (Rosa26-CreER^{T2};Trim71$^{−/−}$) and respective control mESCs (Rosa26-CreER^{T2};Trim71$^{cond/cond}$) were generated as previously described[26].

Mouse MRI.

Structural MR imaging data were collected on an 11.7-T preclinical Bruker magnet using an in-house-built saddle coil for optimal whole brain sensitivity. Mice were anesthetized with isoflurane (3% induction, 1–2% maintenance, in a medical air and oxygen mixture 1:0.5). During imaging, body temperature was maintained with a circulating water bath. We used a Rapid Acquisition with Relaxation Enhancement (RARE) imaging sequence. In 31 minutes and 30 seconds, using a TR/TE of 4,500/11.25 ms, 20 repetitions and RARE factor 8, we obtained a coronal $0.07 \times 0.30 \times 0.07$ mm^3 image of the whole brain (field of view $1.40 \times 8.40 \times 12.0$ mm^3). This sequence was repeated, and the data were averaged after motion correction using customized modules within BioImage Suite (BIS) Web (www.bioimagesuite.org) developed in-house and available free online. In post-processing, again using BIS, we used signal intensity thresholding to delineate the ventricles from surrounding brain tissue and computed ventricular volume.

Mouse tissue preparation and immunostaining.

Mouse brains or embryos at indicated time points (E9.5, E12.5, P0 and P7) were dissected and fixed in 4% paraformaldehyde (PFA) in PBS overnight at 4 °C and then cryoprotected in 30% sucrose in PBS for 48 hours. Samples were then mounted in frozen OCT blocks and sectioned by cryostat at 20 µm. Sections were mounted on microscope slides and stored at −80 °C until use. To begin staining, slides containing sections were first thawed at room temperature. Slides were washed by 0.5% PBST and blocked in 10% normal goat serum (NGS) in PBST. Sections were blocked in 10% NGS in PBST at room temperature for 1 hour and then incubated with primary antibodies diluted in 2.5% NGS in PBST at 4 °C overnight. After primary antibody incubation, sections were washed and incubated with Alexa Fluor-conjugated secondary antibodies (1:500 in 2.5% NGS in PBST) for 1 hour at room temperature. After the final wash, slides were cover-slipped with Prolong Gold Antifade mounting medium. Images were acquired using a Zeiss LSM 800 confocal microscope.

The following primary antibodies (with dilutions) were used: rabbit anti-MIK67 1/250 (Cell Signaling Technology, 9129S), rabbit anti-pH3 1/250 (Cell Signaling Technology, 3377S), chicken anti-DCX 1/500 (Abcam, ab153668), rabbit anti-cleaved caspase 3 Alexa Fluor 488 conjugate 1/500 (Cell Signaling Technology, 9669S), rat anti-BCL11B/CTIP2 1/500 (Abcam, 18465), rabbit anti-POU3F2/BRN2 1/500 (Cell Signaling Technology, 12137S), rabbit anti-TBR1 Alexa Fluor 647 conjugate 1/500 (Cell Signaling Technology, 45664S), mouse anti-acetylated tubulin antibody 1/500 (Sigma-Aldrich, T7451–200UL), rabbit anti-ARL13B 1/500 (Invitrogen, PA5–61840), rabbit anti-S100B 1/200 (Novus, NB200–538), mouse anti-FoxJ1 1/500 (Invitrogen, 14–9965-82), mouse anti-E-cadherin 1/500 (R&D Systems, MBA7481), rabbit anti-OTX2 1/200 (Abcam, 183951), rabbit anti-TRIM71 1/500 (gift from Shinya Yamanaka, Gladstone Institute of Cardiovascular Disease)[33], rabbit anti-pNKCC1 1/500 (Millipore, ABS 1004), rabbit anti-NKCC1 1/500 (Cell Signaling

Technology, 85403S), rabbit anti-pSPAK 1/250 (Millipore, 07–2273) and mouse anti-SPAK 1/200 (Santa Cruz Biotechnology, sc-517361).

All secondary antibodies were purchased from Invitrogen, and the following were used: goat anti-chicken IgY (H+L) Alexa Fluor 555 (A-21437), goat anti-rat IgG (H+L) Alexa Fluor 555 (A-21434), goat anti-mouse IgG (H+L) Alexa Fluor 488 (A-11001), goat anti-mouse IgG (H+L) Alexa Fluor 555 (A-21422), goat anti-mouse IgG (H+L) Alexa Fluor 647 (A-21235), goat anti-rabbit IgG (H+L) Alexa Fluor 488 (A-11008), goat anti-rabbit IgG (H+L) Alexa Fluor 555 (A-21428) and goat anti-rabbit IgG (H+L) Alexa Fluor 647 (A-21245).

RNAscope assay.

RNAscope in situ hybridization was performed using the RNAscope Multiplex Fluorescent v2 Reagent Kit (ACDBio, 323100) according to the manufacturer's directions for fixed-frozen tissue samples. In brief, 14-μm PFA-perfused cryosections were baked for 30 minutes at 60 °C, post-fixed using 4% PFA and ethanol and then treated with H_2O_2 for 10 minutes at room temperature. Target retrieval was performed for 20 minutes at 85 °C, followed by Protease III treatment for 30 minutes at 40 °C. Lin41 probes (ACDBio, 561371-C2) were hybridized for 2 hours at 40 °C, followed by signal amplification and detection according to the manufacturer's instructions. The slides were counterstained with DAPI.

Ependymal cell cultures were briefly fixed with 4% PFA; serially dehydrated in a 50%, 70% and 100% ethanol series; and stored at −20 °C. After rehydration, cells were treated with Protease III for 30 minutes at 40 °C before proceeding with hybridization and amplification as above.

Intracranial pressure measurements.

A pressure sensor probe (Millar's SPR1000 Mikro-Tip mouse pressure catheter) inserted into a water-filled 30-gauge needle and sealed by Tuohy–Borst adaptor to create a closed pressure system was used for the intracranial pressure (ICP) measurements. Specifically, the Millar probe measures pressures in the range of 0.2–8.0 mmHg, which is equal to 2.7–108 mmH_2O. To counterbalance gravity pulling out the liquid inside the 30-gauge needle and creating negative pressure, thereby inducing ICP errors, the height of the water column inside the Tuohy–Borst adaptor was determined not to exceed 10~13 mmH_2O. The pressure sensor was pre-calibrated with another pressure sensor (ADInstruments) for a range between 0 mmHg and 30 mmHg. P7 mouse pups were anesthetized with 2–3% isoflurane; their heads were fixed on a stereotactic frame; and the translucent skull cap was exposed. Using a stereotaxic frame, the 30-gauge needle connected to the pressure sensor was inserted perpendicularly into the lateral ventricles. To record changes in ICP, the pressure sensor was connected to a bridge amplifier (ADInstruments), increasing the signal sensitivity and amplifying the measurement. ICP was recorded for 4 minutes after stabilization of the signal, and the average pressure was calculated over the last 2 minutes of recording. All animals were euthanized at the conclusion of the measurement. The analog voltage measured data were converted to digital data with a 1,000-Hz sampling rate after amplification and low-pass filtering circuit embedded in the electrical circuits (LabChart version 8, ADInstruments). The digital data were transferred to a computer (Intel(R) Core i7–8700 CPU at 3.20 GHz and 16 GB of RAM) through a standard serial communication protocol, and the calibration curve was used to derive the corresponding pressure values.

Live imaging of bulk CSF flow.

Neonatal mouse pups were first anesthetized with isoflurane. Next, 0.5 µl of 1% Evans blue (diluted in 1× PBS) was unilaterally injected into a forebrain ventricle. Immediately after injection, animals were placed inside the IVIS Lumina X5 Imaging System for fluorescent imaging using the Alexa Fluor 647 setting (PerkinElmer). Fluorescence intensity (mean density) was analyzed by selecting regions of interest (ROIs) corresponding to the hindbrain or spinal cord regions in FIJI.

OCT imaging of cilia-driven CSF flow and analysis.

Coronal brain sections (~0.5 mm thick, hand sliced using a sharp blade) collected from freshly dissected brains of mice were placed in a clay-filled Petri dish. The dish was then filled with Leibovitz’s L-15 medium to hydrate the brain samples (Thermo Fisher Scientific). We used a Thorlabs Ganymede 900 nm SD-OCT Imaging System, which allows for 1.4-mm imaging depth in air + water and −2.2-µm axial resolution in water. Polystyrene beads diluted in 1× PBS were added onto the brain explants. We obtained two-dimensional (2D) cross-sectional images by scanning at 36 kHz (36,000 A-scans per second) with maximal 101-dB sensitivity, as previously described[37]. Flow velocimetry was achieved using automated detection and tracking of particles, followed by velocity averaging. Mosaic Particle Tracker plugin built-in ImageJ 2D tracking was used for automated detection of particles and their trajectories[77,78]. The ROI was segmented manually using the MATLAB tool CROIEditor to exclude any particles tracked outside the ventricular space. All particle tracking data outside of the ROI was removed before further analysis. Trajectories were averaged across all frames of each sample to yield mean flow vectors at each pixel position. For visualization purposes, average flow velocity was calculated for 10 × 10-pixel non-overlapping windows. Velocity magnitudes above the 97th percentile were considered outliers resulting from incorrect particle tracking and were removed from further analysis. The number of particles was calculated as the mean number of particles detected across all frames and was normalized using the sample’s ROI area. All image and data processing was performed using MATLAB (MathWorks, version R2019a) and ImageJ (National Institutes of Health, version 1.5.3c).

To validate that observed bead flow is indeed driven by motile cilia, we imaged bead flow in adult ventricular explants (from 6-month-old C57/BL6 WT mice) after applying ciliobrevin toxin (Cayman Chemical, 22587) to adult ventricular explants. Bead flow in toxin condition was compared to that of toxin-naive condition and after washout with 1× PBS.

AFM.

AFM measurements of cortex elastic and viscoelastic properties were performed using an Asylum Cypher ES atomic force microscope (Asylum Research). We used tipless PNP-TR-TL probes (NanoWorld) upon which we attached 20-µm-diameter polystyrene beads (Sigma-Aldrich) with UV curable glue. The spring constant of the probes was calibrated using the thermal method. Slices of brain cortex were placed on a mica substrate and hydrated with Leibovitz's L-15 medium. Viscoelastic properties were measured as previously described[42]. In brief, the atomic force microscope was operated in indentation mode. To measure the force relaxation modulus, the probe was ramped to an indentation depth of 5 µm over 1 second. The indentation was maintained for 20 seconds and then retracted over 1 second. The force relaxation modulus was calculated from the measured force exerted by the probe:

$$G_R(t) = \frac{3}{16\sqrt{R\delta_0^{3/2}}} F(t) \tag{1}$$

where R is the probe radius (constant value of 10 µm), δ_0 is the indentation depth (constant value of 5 µm) and F(t) is the time-dependent force measured during the 20-second indentation. The reported force relaxation modulus was taken at 20 seconds.

The apparent elastic modulus was extracted from the same dataset. However, whereas the force relaxation modulus was extracted from the 20 seconds during which the 5-µm indentation was maintained, the apparent elastic modulus was computed using the first 1-second ramp from 0 µm to 5 µm indentation as follows[41]:

$$E(d) = \frac{3\left(1 - \nu^2\right)}{4\sqrt{R\delta^3}} F(\delta) \tag{2}$$

where ν is the Poisson's ratio of the brain cortex (constant value of 0.5). The reported elastic modulus was taken at an indentation depth of 5 µm.

To measure the creep compliance, the AFM was operated to maintain a constant applied force. The probe was ramped from an applied force of 0 nN to 5 nN over 1 second. The 5-nN load was maintained for 20 seconds, after which the load was reduced to 0 nN over 1 second, and the probe was withdrawn. The creep compliance was calculated from the measured indentation depth:

$$J_C(t) = \frac{16\sqrt{R}}{3F_0} \delta^{3/2}(t) \tag{3}$$

Here, F_0 is the 5-nN applied force. The reported creep compliance was taken at 20 seconds.

Integrative genomic prediction of TRIM71 targets.

To identify putative functional targets and interactors of TRIM71, we used Pearson correlation to identify the top 100 genes correlated with *TRIM71* and top 100 genes anti-correlated with *TRIM71* using the PsychENCODE scRNA-seq dataset of prenatal human brain[12].

Rare damaging mutations were called in *TRIM71* target genes from CH patients with WES as described previously[7]. Specifically, DNMs were called as described above. Transmitted or unphased heterozygous variants were filtered by minor allele frequency (MAF) ≤ 5 ×

10^{-3} in BRAVO and in-cohort MAF ≤ 5×10^{-3}. Only damaging variants that are either LoF (defined as splice-site, stop-gain, stop-loss or frameshift indels) or D-mis (defined as missense variants predicted as deleterious by MetaSVM or have an MPC score ≥2) were considered. To further prioritize heterozygous variants that are potentially damaging to the disease, only variants falling into genes intolerant of monoallelic LoF variants (pLI ≥ 0.9) were kept. Recessive variants, including homozygous and compound-heterozygous variants, were called from trio samples and filtered by MAF ≤ 1×10^{-3} in BRAVO and in-cohort MAF ≤ 5×10^{-3}. Only LoF, D-mis or non-framshift indels were considered. Hemizygous variants were called from male patients and were filtered by MAF ≤ 5×10^{-3} in BRAVO and in-cohort MAF ≤ 5×10^{-3}. Only LoF or D-mis variants were kept. Low-quality variants were filtered out as described previously[7].

Cell culture.

mESCs were cultured on gelatin-coated dishes in mESC medium (KnockOut DMEM (Gibco) supplemented with 15% FCS (Hyclone), non-essential amino acids (Gibco), GlutaMAX (Gibco), penicillin–streptomycin (Gibco), 2-mercaptoethanol (Thermo Fisher Scientific) and LIF (supernatant from L929 cells)) and 2i (3 uM CHIR99021 and 1 uM PD0325901). For neural differentiation with N2B27 medium, mESCs were dissociated with StemPro Accutase Cell Dissociation Reagent (Thermo Fisher Scientific) and washed once, and 400,000 cells were cultured per 12 wells (gelatin coated) in N2B27 medium (50% DMEM/F12 (Gibco), 50% neurobasal (Gibco), B27 supplement (Gibco), N2 supplement (Gibco), penicillin–streptomycin (Gibco), GlutaMAX (Gibco), non-essential amino acids (Gibco) and 50 μg ml^{-1} of BSA (fraction V)) for 2, 4 or 6 days.

HEK293T cells were cultured in DMEM supplemented with 10% FCS and 1% penicillin–streptavidin solution. All cells were grown at 37 °C in a controlled atmosphere with 5% CO_2 and 95% relative humidity.

Generation of FLAG-tagged mESC lines with CRISPR–Cas9.

CRISPR–Cas9 gene editing was used to integrate a FLAG-tag at the N-terminus of TRIM71 in mESC lines (FLAG-TRIM71-WT and FLAG-TRIM71$^{R595H/R595H}$). Potential target guide RNA sequences near the translation start codon (ATG) were identified using the online tool CHOPCHOP (https://chopchop.cbu.uib.no). The protospacer sequence (5′-CCGGGAACGAAGCCATTTGCAGG-3′) was cloned into the plasmid pSpCas9(BB)-2A-Puro (PX459), which was a gift from Feng Zhang (Addgene plasmid 48139) following the Zhang lab Target Sequence Cloning Protocol[79]. The repair template for homology-dependent repair was cloned using the In-Fusion HD Cloning Plus Kit (Takara Bio) with four fragments with overlapping sequences: (1) linearized pCDNA3.1; (2) and (3) PCR produced 3′-/5′-homology arms; and (4) synthesized DNA fragment carrying the FLAG-sequence. mESCs (Trim71$^{cond/cond}$ or Trim71$^{R595H/R595H}$) were co-transfected with both plasmids using Lipofectamine 2000 reagent. Twenty-four hours after transfection, mESCs were selected by addition of 1 ug ml^{-1} of puromycin. Surviving cells were released from puromycin selection after another 48 hours and left in mESC medium until colonies were visible by eye. Colonies were picked and expanded. Insertion of the FLAG-tag was confirmed by genotyping and FLAG-Co-IP followed by immunoblotting.

UV-crosslink RNA immunoprecipitation (CLIP).

Two confluent 10-cm dishes of HEK293T cells were transfected with either pRK5-Flag-TRIM71 (WT, d6NHL, R608H, R796H, empty) overexpression plasmids. Forty-eight hours after transfection, cells were washed with ice-cold PBS and irradiated with UV light at 300 mJ cm^{-2}. For CLIP with mESCs (FLAG-TRIM71-WT, FLAG-$TRIM71^{R595H/R595H}$ and TRIM71-WT (control)), two confluent 15-cm dishes of each condition were irradiated with UV light at 300 mJ cm^{-2}. Cells were harvested and lysed in 500 µl of RNA-IP buffer (20 mM Tris-HCl pH 7.4, 100 mM KCl, 5 mM $MgCl_2$, 0.2% NP-40), supplemented with 120 U ml^{-1} of RNase inhibitor (RiboLock, Thermo Fisher Scientific) and protease inhibitors (PMSF, antipain, benzamidin, leupeptin and aprotinin). Cell lysates were cleared by centrifugation (16,100*g*, 4 °C). Protein concentrations were estimated using the Pierce BCA assay kit (Thermo Fisher Scientific) and adjusted. Next, 20 µg of total protein lysate was retained as protein-Input for immunoblotting, and 50 µl was retained for RNA-Input. Then, 2 mg of protein lysates was incubated with 50 µl of anti-FLAG M2 Magnetic Beads (Sigma-Aldrich) overnight at 4 °C on a rotating wheel. After five washing steps with RNA-IP buffer, beads were divided for immunoblotting (20%) and for qRT–PCR (80%). Beads for qRT–PCR were incubated with Proteinase K (Peqlab) for 30 minutes at 37 °C before RNA extraction. Immunoblotting, RNA extraction and qRT–PCR were performed as described below.

Specific enrichments were determined after qRT–PCR from cycle threshold (CT) values for each construct over total RNA by:

$$\text{Enrichment} = 2^{\wedge} - \left[\left(CT_{\text{CLIP\_target}} - CT_{\text{CLIP\_ref}}\right) - \left(CT_{\text{Input\_target}} - CT_{\text{Input\_ref}}\right)\right]$$

where the CT values of $CT_{\text{CLIP\_target}}$ corresponds to the CLIP enrichment of the gene of interest; $CT_{\text{CLIP\_ref}}$ corresponds to the CLIP enrichment of the gene of housekeeping (here, 18S rRNA was used); and $CT_{\text{Input\_target}}$ and $CT_{\text{Input\_ref}}$ correspond to the Input, respectively.

Specific enrichments of each condition were finally normalized to the WT TRIM71 condition.

RNA extraction, cDNA synthesis and qRT–PCR.

TRIzol reagent (Thermo Fisher Scientific) was used according to the manufacturer’s instructions. In brief, samples were resuspended in 500 µl of TRIzol reagent, mixed with 100 µl of chloroform and centrifuged (13,400*g*, 4 °C) for 5 minutes. The upper aqueous phase was transferred to a new cap, and nucleic acids were precipitated by adding 250 µl of isopropanol followed by centrifugation (13,400*g*, 4 °C) for 10 minutes. The pellet was washed once with 70% ethanol, dried at 37 °C and resolved in RNase-free water. DNA was digested with 1 U of DNAseI (1 U μl^{-1}) for 30 minutes at 37 °C after heat inactivation for 10 minutes at 75 °C.

RNA concentrations were determined spectrophotometrically and reverse transcribed using the High Capacity cDNA Reverse Transcription Kit (Applied Biosystems) according to the manufacturer’s instructions. For Input and normal RNA samples, 1 µg of cDNA was synthesized; for CLIP samples, the complete RNA was used.

qRT–PCR was performed using either TaqMan or SYBR Green assays (Bio-Rad) on a Bio-Rad qCycler. The following TaqMan probes and qRT–PCR primers were used:

TaqMan gene expression assays:

CDKN1A (Hs00355782_m1), Cdkn1a (Mm04205640_g1), Inhbb (Mm03023992_m1), Gapdh (Mm99999915_g1), Trim71 (Mm01341471_m1). qRT–PCR Primer:

qHs_EGR1-fw: CCTGACCGCAGAGTCTTTTC

qHs_EGR1-rv: AGCGGCCAGTATAGGTGATG

qMm-Egr1-for: ACCACAGAGTCCTTTTCTGACA

qMm-Egr1-rev:TGAAAAGGGGTTCAGGCCAC

qMm-Spred1-for:AGAAGCTCAGACATAAGACCGT

qMm-Spred1-rev:ATGTCTAGGCCTTGCTGACT

qMm-Cbfa2t2-for: CTCAGGCAGAGGGTCGAAG

qMm-Cbfa2t2-rev:GGCACCCTTTTCTCACAACC

qMm-Tcf4-for:TAGGGAAAGCCCTAGCTTCG

qMm-Tcf4-rev:GCCTGCTGAGAGTGAAGGAG

qMm-Crebbp-for:CATTGTCAGGCTGGGAAAGC

qMm-Crebbp-rev:AAAGGGAGGCAAACAGGACA

qMm-Bcl11b-for:GAATAGATGCCGGGGCAATG

qMm-Bcl11b-rev:ATGGTAGCCTCCACATGGTC

q-18S-rRNA-fw: GTAACCCGTTGAACCCCATTC

q-18S-rRNA-rv: CCATCCAATCGGTAGTAGCGAC

Immunoblotting.

Adjusted protein lysates were supplemented with loading buffer (12% glycerol, 60 mM Na_2EDTA pH 8, 0.6% SDS, 0.003% bromphenol blue) and denatured for 10 minutes at 95 °C before SDS-PAGE. Proteins were wet-transferred to a nitrocellulose membrane at 80 V for 2 hours in transfer buffer (25 mM Tris-HCl pH 7.6, 192 mM glycine, 20% methanol, 0.03% SDS). Membranes were blocked in 5% milk powder diluted in TBST (50 mM Tris-HCl pH 7.6, 150 mM NaCl, 0.05% Tween 20), before an overnight incubation at 4 °C with the primary antibodies. After three times washing with TBST, membranes were incubated with HRP-coupled secondary antibodies for 1 hour at room temperature, followed by another three washes with TBST. Blots were developed with Pierce ECL Substrate Kit following the manufacturer's instructions. The following antibodies were used: anti-FLAG M2 (mouse, F1804, Sigma-Aldrich), anti-GAPDH (mouse, ACR001P, Acris), anti-TRIM71 (rabbit, kind gift from the Yamanaka lab), anti-TRIM71 (rabbit, PAB19293, Abnova), anti-SHCBP1 (rabbit, 12672–1-AP, Proteintech), anti-Cdkn1a/p21 (rabbit, 2947, Cell Signaling Technology), anti-EGR1 (rabbit, 4154, Cell Signaling Technology), anti-UPF1 (rabbit, 9435, Cell Signaling Technology), anti-VINCULIN (mouse, V9131, Sigma-Aldrich), anti-ubiquitin (rabbit, 3933, Cell Signaling Technology) and anti-tubulin (mouse, T9026, Sigma-Aldrich).

Proliferation assay.

To monitor cell division of mESCs upon steady state or upon neural differentiation, cells were labeled with the Cell Proliferation Dye eFluor 670 (Thermo Fisher Scientific) according to manufacturer instructions. In brief, mESCs were dissociated, counted and washed in PBS. In total, 1.4 million cells were stained with the proliferation dye eFluo 670 diluted to 5 μM in 1 ml of PBS by incubation for 10 minutes at 37 °C. Staining reaction was stopped by the addition of 5 ml of FCS and incubation for 5 minutes on ice. Cells were pelleted, washed once with medium and cultured in N2B27 for neural differentiation. In total, 400,000 cells were cultured in three wells of a 12-well plate, one well for each time point. The remaining cells were used for flow cytometry (BD FACSCanto II) to measure the initial fluorescence intensity, later used as time point day 0. Cells were dissociated at indicated time points (days 2, 4 and 6), and fluorescence reduction was measured by flow cytometry. The number of cell divisions was calculated assuming half decrease of the median fluorescence intensity upon each cell division with the following formula:

$$\text{Division Number} = \log_2\left[\left(\text{MFI}_{\text{day0}} - \text{MFI}_{\text{unstained}}\right)/\left(\text{MFI}_{\text{dayX}} - \text{MFI}_{\text{unstained}}\right)\right]$$

Dual luciferase reporter assays.

HEK293T cells in 12-well plates were co-transfected with the specific psiCHECK2 dual luciferase plasmid and the specified pRK5-Flag-TRIM71 (WT, d6NHL, R608H, R796H, empty) overexpression plasmids in a 1:4 ratio. The psiCHECK2 plasmids contained a specific 3′ UTR sequence downstream Renilla luciferase coding sequence and an additional open reading frame coding for Firefly luciferase under a different promotor as a normalization control. As control condition, psiCHECK2 with no insert was used (Renilla-empty). Cells were harvested 48 hours after DNA transfection in 1× passive lysis buffer. Renilla and Firefly luminescence were measured in a luminometer using the Dual Luciferase Reporter Assay Kit, following the manufacturer's instructions (Promega). The data were analyzed by calculating the ratio of Renilla-3′ UTR/Firefly and normalizing to the Renilla-empty/Firefly ratio. The results are represented in normalized relative light units.

PAR-CLIP.

mESCs expressing FLAG-TRIM71-WT, FLAG-TRIM71$^{R595H/R595H}$, or TRIM71-WT were grown to confluency on a 10 ×15 cm dish. mESCs were treated with 250 uM 4-thiouridine in mESC medium overnight. After a single wash with PBS, cells were cross-linked on ice at 312 nm for 5 minutes, scraped and collected in PBS. Cell pellets were shock-frozen in liquid nitrogen.

PAR-CLIP was performed as previously described[80]. Cells were resuspended in 3 volumes (v/v(pellet)) of RIPA buffer (10 mM Tris-HCl (pH 8.0), 1 mM EDTA, 0.5 mM EGTA, 1% Triton X-100, 0.1%, sodium deoxycholate, 0.1% SDS, 140 mM NaCl, 1× complete EDTA-free protease inhibitor mixture (Roche)) and sonicated in a Bioruptor Pico (Diagenode) with the following settings: three times 30 seconds ON and 30 seconds OFF at 4 °C. The lysate was cleared by centrifugation at 13,000*g* for 15 minutes at 4 °C. The lysate was treated with 1 U μl^{-1} of RNase T1 (Thermo Fisher Scientific) for 15 minutes at 21 °C. TRIM71 was immunoprecipitated using 10 $\mu l\ ml^{-1}$ of lysate ('bead volume') anti-Flag magnetic beads (M2, Sigma-Aldrich) on a rotating wheel for 2 hours at 4 °C. Beads were washed three times with 1 ml of IP wash buffer (20 mM Tris, pH 7.5, 150 mM NaCl, 2 mM EDTA, 1% (v/v) NP40, 1× complete EDTA-free protease inhibitor mixture (Roche)) and resuspended in 1 bead volume of IP wash buffer. A second RNase T1 digestion was performed with 0.5 U μl^{-1} for 15 minutes at 21 °C in IP wash buffer. The beads were washed two times in 1 ml of high-salt wash buffer (20 mM Tris pH 7.5, 500 mM NaCl, 2 mM EDTA, 1% (v/v) NP40), two times in 1 ml of RIPA and two times in dephosphorylation buffer (50 mM Tris-HCl pH 7.9, 100 mM NaCl, 10 mM $MgCl_2$). Beads were resuspended in 1 bead volume of dephosphorylation buffer. The ends of the TRIM71-bound RNA fragments were dephosphorylated using 0.5 U μl^{-1} of calf intestinal phosphatase (New England Biolabs) for 10 minutes at 37 °C with shaking at 800 r.p.m. Beads were washed two times in PNK wash buffer (100 mM Tris-HCl pH 7.5, 20 mM $MgCl_2$) and resuspended in 1 bead volume of PNK buffer (70 mM Tris-HCl pH 7.5, 10 mM $MgCl_2$, 5 mM DTT). The 5′ end of the RNA was radioactively labeled using 1 U μl^{-1} of T4 polynucleotide kinase (New England Biolabs) and 0.5 μCi μl^{-1} ^{32}P-γ-ATP (PerkinElmer) for 30 minutes at 37 °C. Then, 100 μM ATP was added, and incubation was extended for 5 minutes to achieve quantitative 5′ end phosphorylation. The beads were washed five times with 800 μl of PNK wash buffer. Beads were resuspended in 30 μl of 2× SDS-PAGE loading buffer and incubated for 5 minutes at 95 °C. Beads were then placed on a magnetic rack, and the supernatant was transfered to a new tube.

The protein–RNA complexes were separated next to pre-stained protein standard (Bio-Rad) by a 4–12% NUPAGE gel (Invitrogen) at 200 V for 60 minutes. The RNA–protein complexes were visualized by autoradiography on a Typhoon FLA 7000 (GE Healthcare).

SHCBP1-immunoprecipitation.

For SHCBP1-immunoprecipitation (IP), neurogenesis was induced in mESCs (Trim71-KO, Trim71$^{fl/fl}$, Trim71-WT, Trim71$^{R595H/R595H}$) by RA. In total, 200,000 mESCs were seeded in a 6-cm dish and cultured for 24 hours in mESC medium. Medium was changed to DMEM (PAN Biotech), 10% FCS, GlutaMAX (Gibco), penicillin–streptomycin (Gibco) and

2-mercaptoethanol (Thermo Fisher Scientific), supplemented with 5 µM RA and cultured for three additional days. Cells were harvested and lysed in RIPA buffer + protease inhibitors (PMSF, antipain, benzamidin, leupeptin and aprotinin) for 20 minutes on ice, and the cell lysate was cleared by centrifugation (5 minutes, 4 °C, 16,000*g*). Protein concentrations were determined by BCA assay (Thermo Fisher Scientific), and samples were adjusted. Dynabeads (Dynabeads Protein G, Thermo Fisher Scientific) were equilibrated in RIPA buffer, and SHCBP1-AK was coupled for 2 hours rotating at 4 °C. For Mock-IP, equilibrated beads without antibody were used. Adjusted protein lysates were divided and added to antibody-coupled beads or to Mock-IP and incubated overnight at 4 °C while rotating. Beads were washed three times with RIPA buffer and eluted in 25 µl of 1× sample buffer. Immunoblotting was performed as described above. Ubiquitin and SHCBP1 levels were detected with respective antibodies. Band quantification was performed with ImageJ and normalized as indicated.

Bulk RNA sequencing.

For bulk RNA sequencing, 40,000 mESCs (Trim71$^{cond/cond}$, Trim71$^{-/-}$, Trim71-WT, TRIM71$^{R595H/+}$ and TRIM71$^{R595H/R595H}$) were seeded in six-well plates and cultured for 2 days in mESC medium + 2i. Cell were harvested and RNA was extracted as described above.

Total RNA was converted into libraries of double-stranded cDNA molecules as a template for high-throughput sequencing following the manufacturer’s recommendations using the Illumina TruSeq RNA Sample Preparation Kit v2 (Illumina, RS-122–2001). In brief, mRNA was purified from 100 ng of total RNA using poly-T oligonucleotide-attached magnetic beads. Fragmentation was carried out using divalent cations under elevated temperature in Illumina proprietary fragmentation buffer. First-strand cDNA was synthesized using random oligonucleotides and SuperScript II (Thermo Fisher Scientific, 18064022). Second-strand cDNA synthesis was subsequently performed using DNA polymerase I and RNase H. Remaining overhangs were converted into blunt ends via exonuclease and polymerase activities, and enzymes were removed. After adenylation of 3′ ends of DNA fragments, Illumina PE adapter oligonucleotides were ligated to prepare for hybridization. DNA fragments with ligated adapter molecules were selectively enriched using Illumina PCR primer PE1.0 and PE2.0 in a 15-cycle PCR reaction. Size selection and purification of cDNA fragments with preferential lengths of 200 bp were performed using SPRI beads (Beckman Coulter, A63881). Size distribution of cDNA libraries was measured using the Agilent high-sensitivity D1000 assay (Agilent, 5067–5585) on a TapeStation 4200 system (Agilent Technologies). cDNA libraries were quantified using KAPA Library Quantification Kits (Kapa Biosystems, KK4854). After cluster generation on a cBot, a 75-bp single-read run was performed on a HiSeq 1500 using TruSeq SBS v3-HS chemistry.

RNA sequencing analysis.

Sequenced reads were aligned and quantified using STAR: ultrafast universal RNA-seq aligner (version 2.7.3a) and the murine reference genome, GRCm38p5, from the Genome Reference Consortium. Raw counts were imported using the DESeqDataSetFromHTSeqCount function from DESeq2 (version 1.26.0) and rlog-transformed according to the DESeq2 pipeline. DESeq2 was used for the calculation of normalized counts for each transcript using default parameters. All normalized transcripts with a maximum over all row mean lower than 20 were excluded, resulting in 13,284 present protein-coding transcripts. Undesired or hidden causes of variation, such as batch and preparation date, were removed using the sva package. The normalized rlog-transformed expression data were adjusted with four surrogate variables identified by sva using the function removeBatchEffect from the limma package. To determine gene clusters, CoCena (Construction of Co-expression network analysis) was calculated based on Pearson correlation on all present genes. Pearson correlation was performed using the R package Hmisc (version 4.1–1). To increase data quality, only significant ($P < 0.05$) correlation values were kept. A Pearson correlation coefficient cutoff of 0.803 (present genes; 10,260 nodes and 69,986 edges) was chosen, resulting in networks following the power-law distribution of $r^2 = 0.934$ (scale-free topology). Unbiased clustering was performed using the ‘leiden modularity’ algorithm in igraph (version 1.2.1). Clustering was repeated 100 times. Genes assigned to more than ten different clusters received no cluster assignment. The mean group fold change expression for each cluster and condition is visualized in the Cluster/Condition heat map. Clusters smaller than 40 genes are not shown.

Gene ontology enrichment analysis.

To test for functional enrichment for all modules and the respective genes, we performed gene ontology enrichment analysis (GOEA) for using the GO set of biological processes. Gene set ‘GO. v5.2.symbols_mouse.gmt’ was obtained from the Molecular Signatures Database. The compareCluster and enrichGo functions from the R package ClusterProfiler (version 3.12.0) were used to determine significant enrichment ($q < 0.05$) of biological processes. All present genes were used as background (universe). To focus only for neurological gene sets, all GO term gene sets were selected for terms including the term ‘neuro’, ‘neural’ and ‘nerv’. Network visualization was performed using the cnetplot function from the R package ClusterProfiler.

Linear support vector regression.

Linear support vector regression was employed to computationally deconvolute the study’s RNA sequencing samples. Gene expression tables were normalized with DESeq2 and were used as the input mixture file. Neuronal development signatures from the dataset PRJNA185305 were generated as described on https://cibersortx.stanford.edu//tutorial.php. The algorithm was subsequently run with 100 permutations, and the proportions of cell types were visualized with ggplot2 (version 3.2.1).

Extended Data

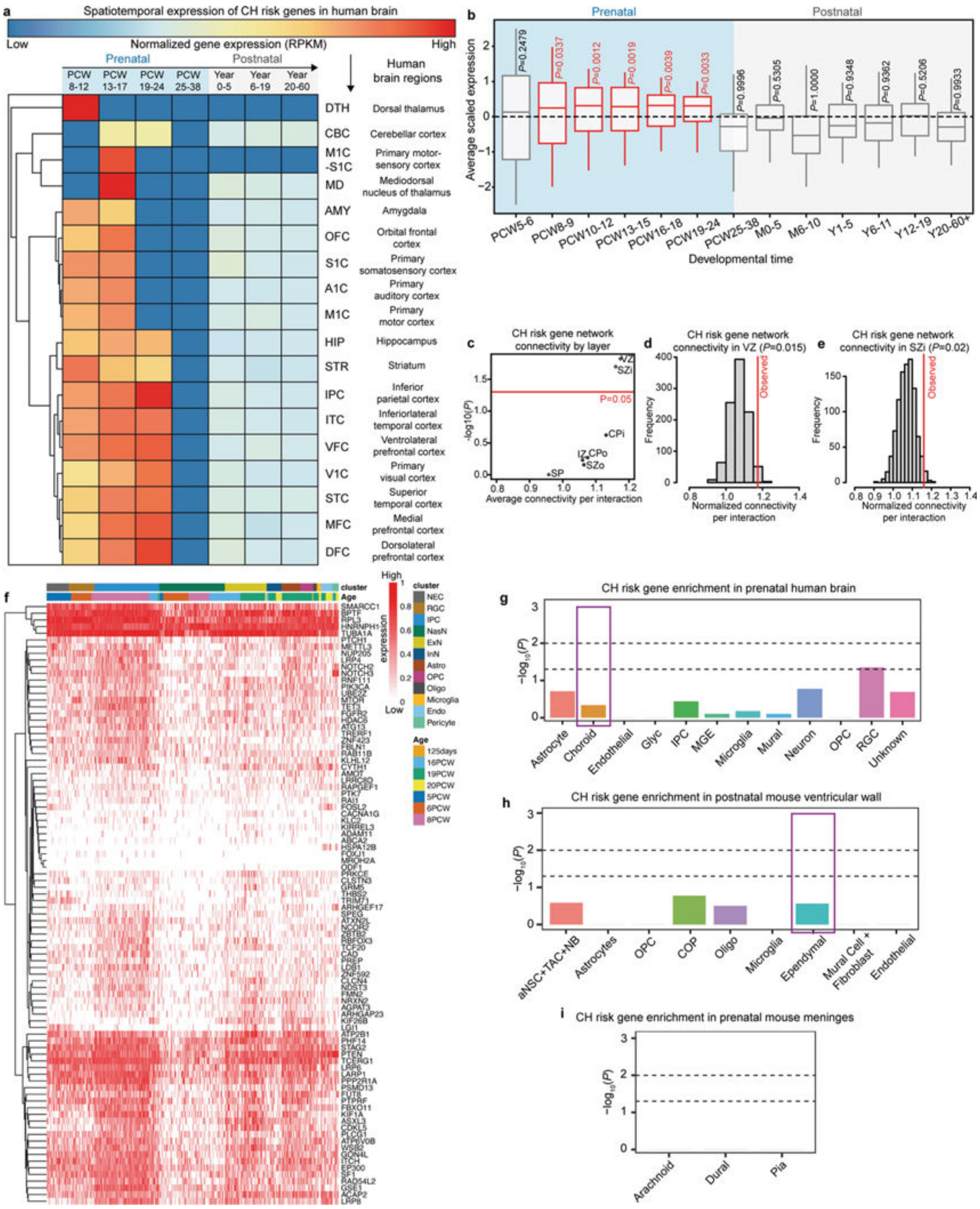

Extended Data Fig. 1 |. Integrative genomic analysis of CH genetic risk.

a) Heatmap showing expression of CH risk genes across developmental timepoints and regions of the developing human brain. Analyzed transcriptomic dataset from[12]. b) Enrichment of CH risk genes across developmental timepoints of the human brain in a microarray dataset of the human brain from[11]. PCW: post-conception week, M: month, Y: year. Boxplot (in f): median (line), 25th and 75th percentiles (box), whiskers extend up to 1.5

times the interquartile range from the top (bottom) of the box to the furthest datum within that distance. Significance was calculated by comparing to background expression using one-sided Wilcoxon rank sum test. For detailed statistical information, see Supplementary Table 13. c-e) CH risk gene network connectivity in different layers of the prenatal human frontal neocortex. Analyzed transcriptomic dataset from[13]. c) VZ- and SVZi-specific CH risk gene interaction networks have the highest average connectivity per interaction. d-e) VZ (d) and SVZi (e) have significantly higher CH risk gene interaction network connectivity than expected by chance. The red line indicates the observed connectivity, and the gray histogram shows the null distribution from 1,000 permutations. P values were calculated by permutation tests (see Methods). f) Heatmap showing maximal expression of CH risk genes across different cell types of the developing human cortex. Analyzed transcriptomic dataset from[12]. g) Enrichment of CH risk genes in a prenatal human brain single-cell RNA sequencing data set from[14]. Purple square highlights lack of enrichment in choroid plexus cells. Choroid: choroid plexus, Glyc: glycolysis, IPC: intermediate progenitor cells, MGE: medial ganglionic eminence, OPC: oligodendrocyte precursor cells, RGC: radial glia cells. P values were calculated by hypergeometric test. h) Enrichment of CH risk genes in a postnatal mouse ventricular wall single-cell RNA sequencing data set from[17]. Purple square highlights lack of enrichment in ependymal cells. aNSC: actively dividing neural stem cells, TAC: transit amplifying cells, NB: neuroblasts, OPC: oligodendrocyte progenitor cells, COP: committed oligodendrocyte precursors. P values were calculated by hypergeometric test. i) Enrichment of CH risk genes in a prenatal mouse meninges single-cell RNA sequencing data set from[18]. P values were calculated by hypergeometric tests.

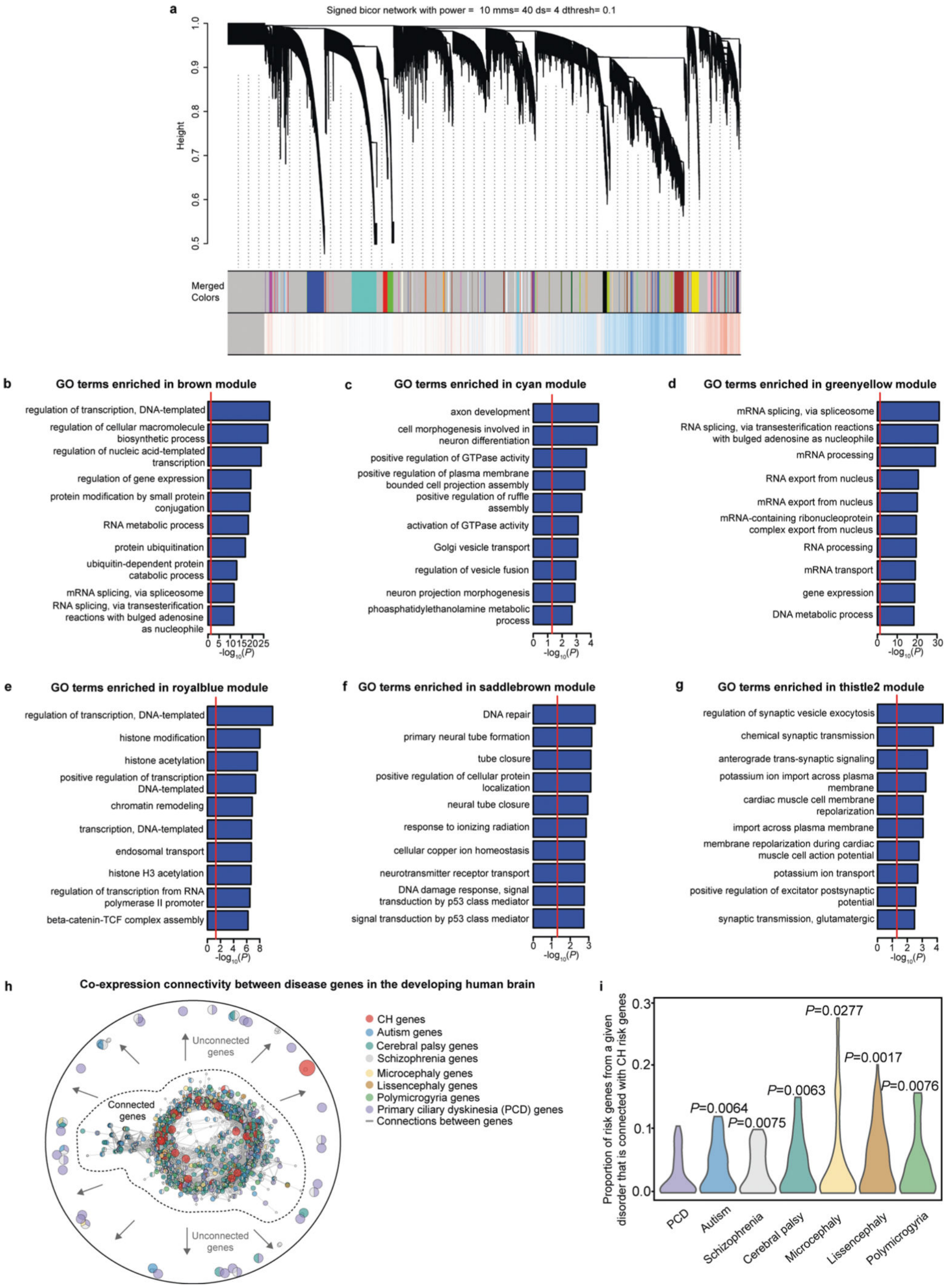

Extended Data Fig. 2 |. Gene co-expression network analysis of CH genetic risk.

a) Clustering dendrogram of genes showing module membership in colors. The y axis represents network distance as determined by 1-topological overlap (TO), where values closer to 0 indicate greater similarity of probe expression. Analyzed transcriptomic dataset from[12]. b-g) GO term enrichment analysis of gene co-expression modules that are enriched for CH risk genes. Significance was calculated by two-sided Fisher's exact test. h-i) Co-expression network connectivity between CH and other developmental disorder risk genes. CH risk genes exhibit greater connectivity to cortical developmental disorder genes than to

PCD genes. Significance was tested using one-sided Wilcoxon rank sum test by comparing to the reference group, CH-PCD.

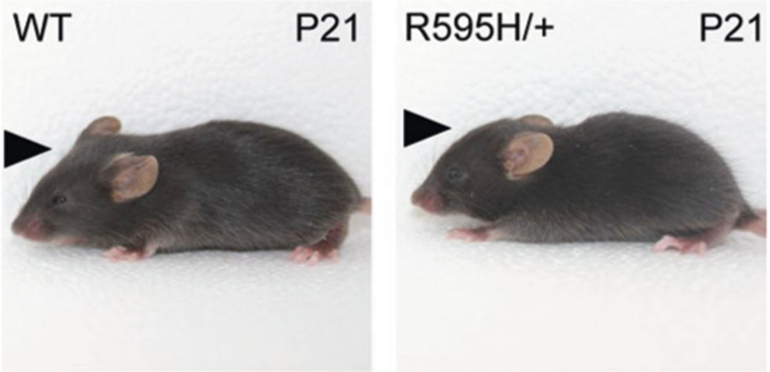

Extended Data Fig. 3 |. Macrocephalic appearance of a hydrocephalic *Trim71*$^{R595H/+}$ mouse compared to a WT control at P21.

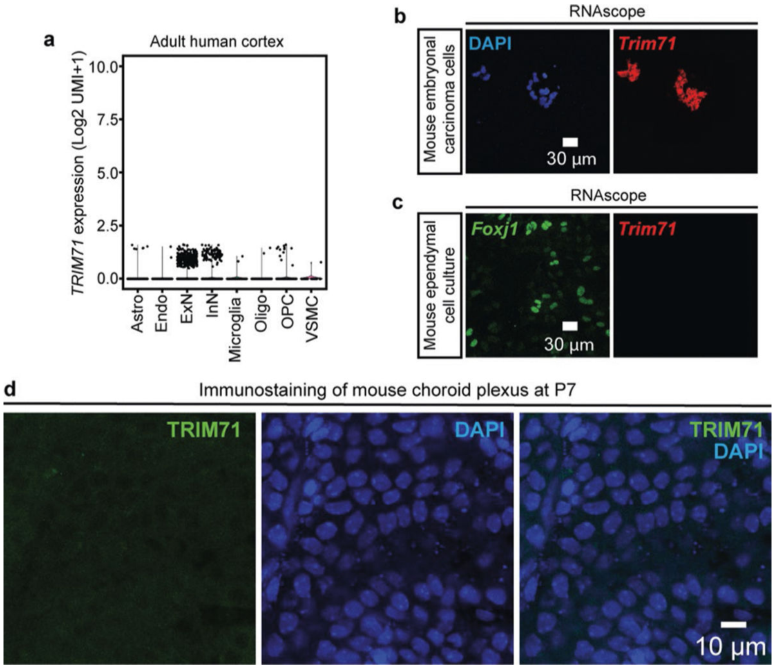

Extended Data Fig. 4 |. Characterization of *TRIM71* expression.

a) *TRIM71* is minimally expressed in the adult human cortex. Analyzed single-nucleus RNA-sequencing data from[12]. b-c) RNAscope *in situ* hybridization of *Trim71* in mouse embryonal carcinoma cells (b) or mouse *Foxj1*-expressing ependymal cell cultures (c) d) TRIM71 immunostaining in the WT mouse choroid plexus at P7.

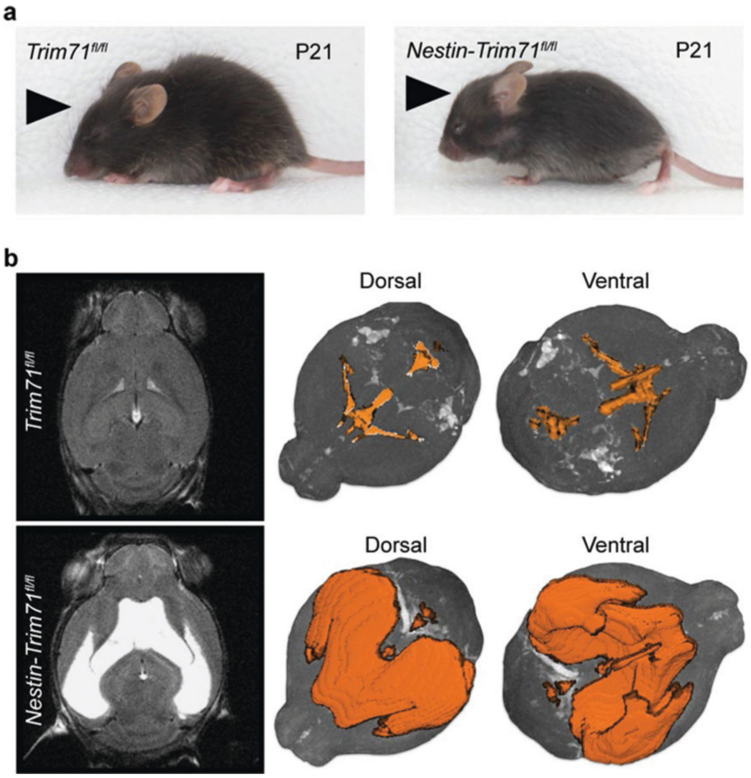

Extended Data Fig. 5 |. Conditional knockout of *Trim71* in embryonic NSCs by *Nestin-Cre* results in hydrocephalus in a subset of mice.

a) A subset of *Nestin-Trim71*$^{fl/fl}$ mice develop hydrocephalus with obvious macrocephaly at P21. b) Brain MRI demonstrates severe ventriculomegaly at P21 in a representative hydrocephalic *Nestin-Cre;Trim71*$^{fl/fl}$ mouse compared to a *Trim71*$^{fl/fl}$ control. 3D reconstructions of the ventricular system based on MRI scans are shown.

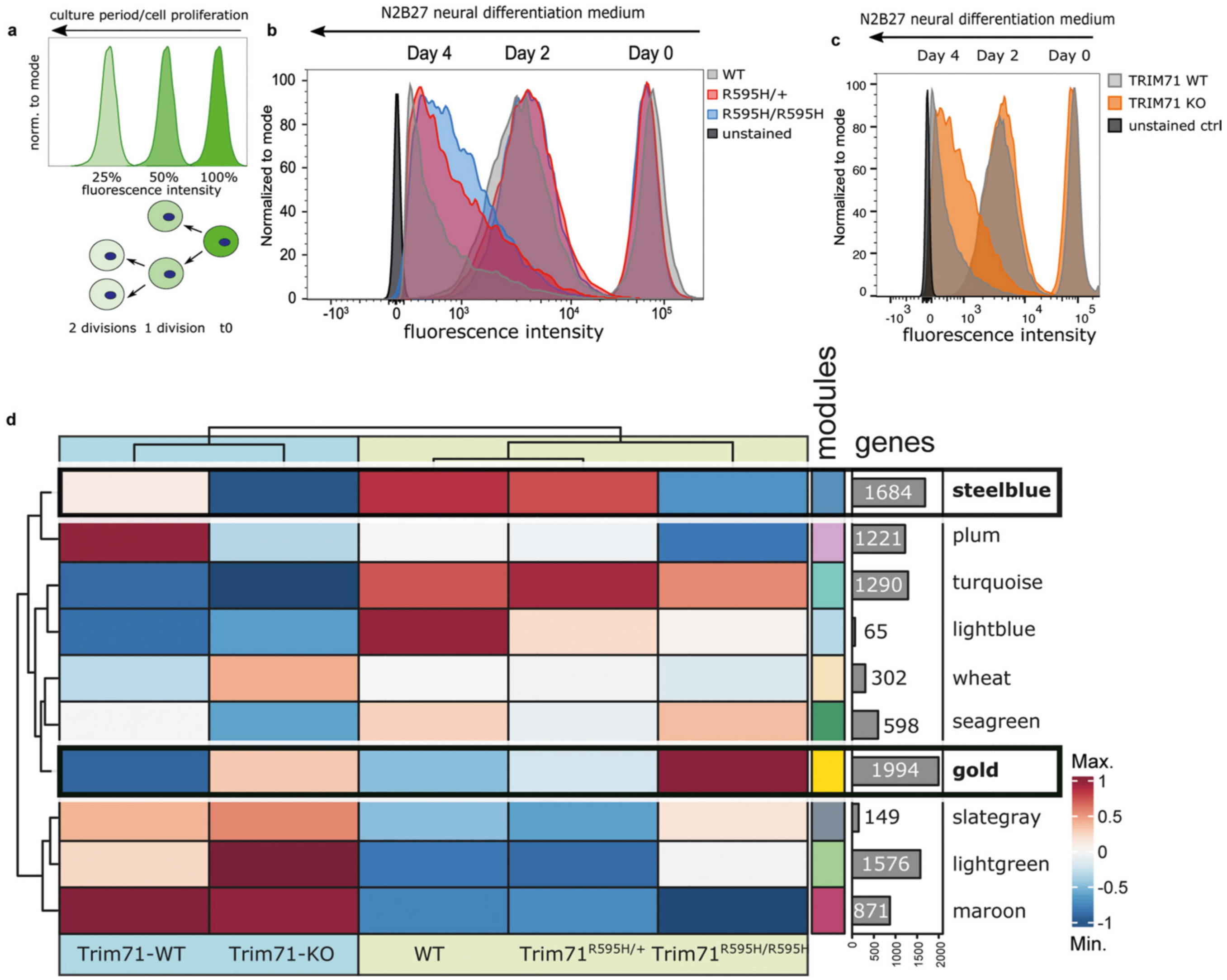

Extended Data Fig. 6 |. Mutant TRIM71 leads to reduced cell proliferation upon neural differentiation and an altered transcriptome.

a) Schematic of experimental paradigm of eFluor670 proliferation assay. Fluorescence intensity decreases by half upon every cell division. b,c) Representative histograms of eFluor670-labelled mESCs undergoing neural differentiation. Proliferation defects in mutant (*Trim71*$^{R595H/+}$, *Trim71*$^{R595H/R595H}$) (b) and *Trim71* KO (c) mESC are reflected by slower loss of fluorescence intensity over time than that in WT or *Trim71*$^{fl/fl}$ control mESCs.

d) Heatmap of the bulk RNA-sequencing showing gene expression profiles clustered in modules over mutant *Trim71* genotypes.

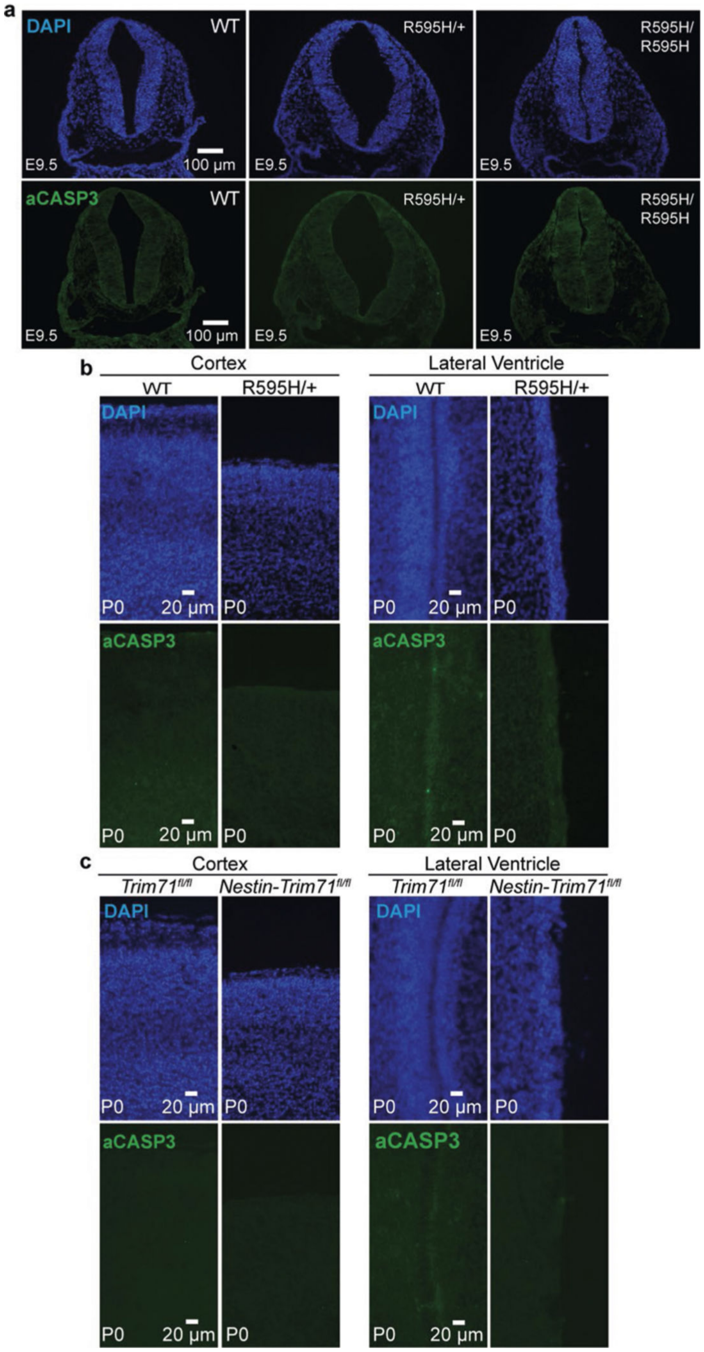

Extended Data Fig. 7 |. Low levels of active caspase 3 (aCASP3) staining in the brains of control and *Trim71* mutant mouse models.

a) aCASP3 staining in the neural tube neuroepithelia of WT, *Trim71*$^{R595H/+}$, and *Trim71*$^{R595H/R595H}$ embryos at E9.5. b) aCASP3 staining in the cortices and lateral ventricles of WT and hydrocephalic *Trim71*$^{R595H/+}$ mice at P0. c) aCASP3 staining in the cortices and lateral ventricles of *Trim71*$^{fl/fl}$ and hydrocephalic *Nestin-Cre;Trim71*$^{fl/fl}$ mice at P0.

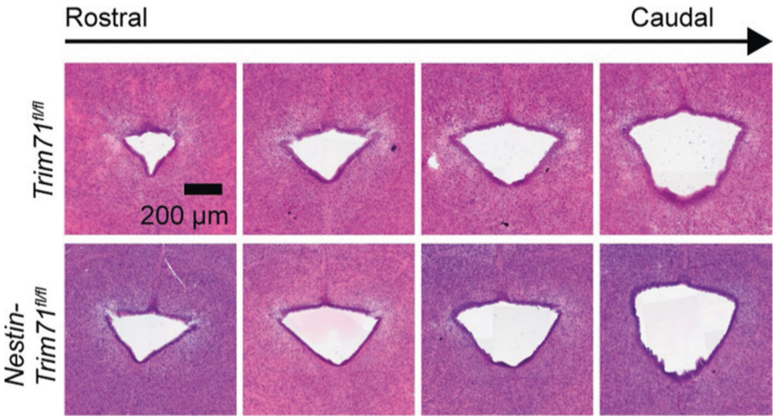

Extended Data Fig. 8 |. H&E stained images of histological sections throughout the rostrocaudal extent of the midbrain cerebral aqueduct in P0 hydrocephalic *Nestin-Trim71*$^{fl/fl}$ mouse and a *Trim71*$^{fl/fl}$

control, demonstrating anatomical patency of the aqueduct in both genotypes.

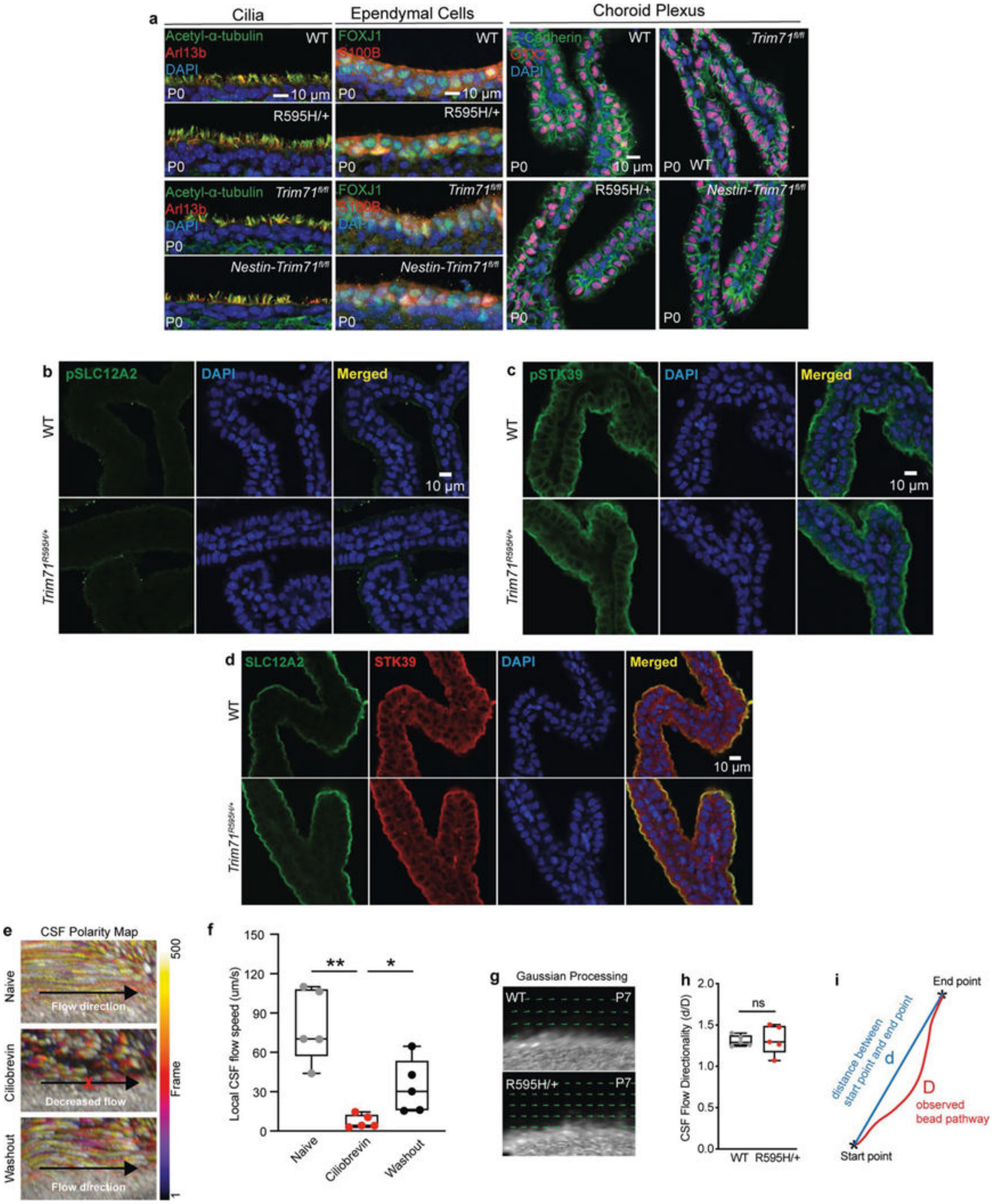

Extended Data Fig. 9 |. Characterization of ependymal cilia and choroid plexus in hydrocephalic *Trim71* mutant mice.

a) Coronal brain sections from control and hydrocephalic mice were stained for ciliary markers (acetyl-α-tubulin and ARL13B), ependymal cell markers (S100B and FOXJ1), and choroid plexus epithelial cell markers (E-Cadherin, OTX2).b-d) Immunostaining for molecular correlates of choroid plexus hypersecretion in WT controls and hydrocephalic *Trim71*$^{R595H/+}$ P0 mice. Immunostaining of phosphorylated SLC12A2/ NKCC1 (pSLC12A2) (b) and phosphorylated STK39/SPAK (pSTK39) (c) in the choroid plexi of a WT control and hydrocephalic *Trim71*$^{R595H/+}$ P0 mouse. d) Immunostaining of SLC12A2/NKCC1 and STK39/SPAK in the choroid plexi of a WT control and hydrocephalic *Trim71*$^{R595H/+}$ P0 mouse. e-f) Validation of OCT imaging platform to characterize ependymal cilia-driven CSF flow *ex vivo*. e). Representative flow polarity maps demonstrating bead trajectories (by temporal color coding) over time in an adult WT mouse brain explant in toxin-naive condition, with ciliobrevin, and after washout of toxin. Color bar represents color versus corresponding frame in the color-coded image. f) Quantitation of local CSF flow speed at the ventricular wall in brain explants from adult WT mouse brains in the different experimental conditions. g-i) CSF flow directionality in WT littermate controls and hydrocephalic *Trim71*$^{R595H/+}$ mice at P7. g) Post-Gaussian processing CSF flow maps in a WT littermate control and hydrocephalic *Trim71*$^{R595H/+}$ mice at P7. h,i) Quantitation of CSF flow directionality in WT littermate controls and hydrocephalic *Trim71*$^{R595H/+}$ mice at P7. Directionality is represented as the distance between the start point and end point (d) divided by the bead pathway (d), see panel (i). Significance was tested by a two-sided paired t-test (f) or two-sided unpaired t-test (h): *: $P<0.05$, **: $P<0.01$, ns (not significant): $P>0.05$. Data represented as boxplots (f,h): median (line), 25th and 75th percentiles (box), whiskers go down to the smallest value and up to the largest, overlaid with individual data points. For detailed statistical information (f, h), see Supplementary Table 13.

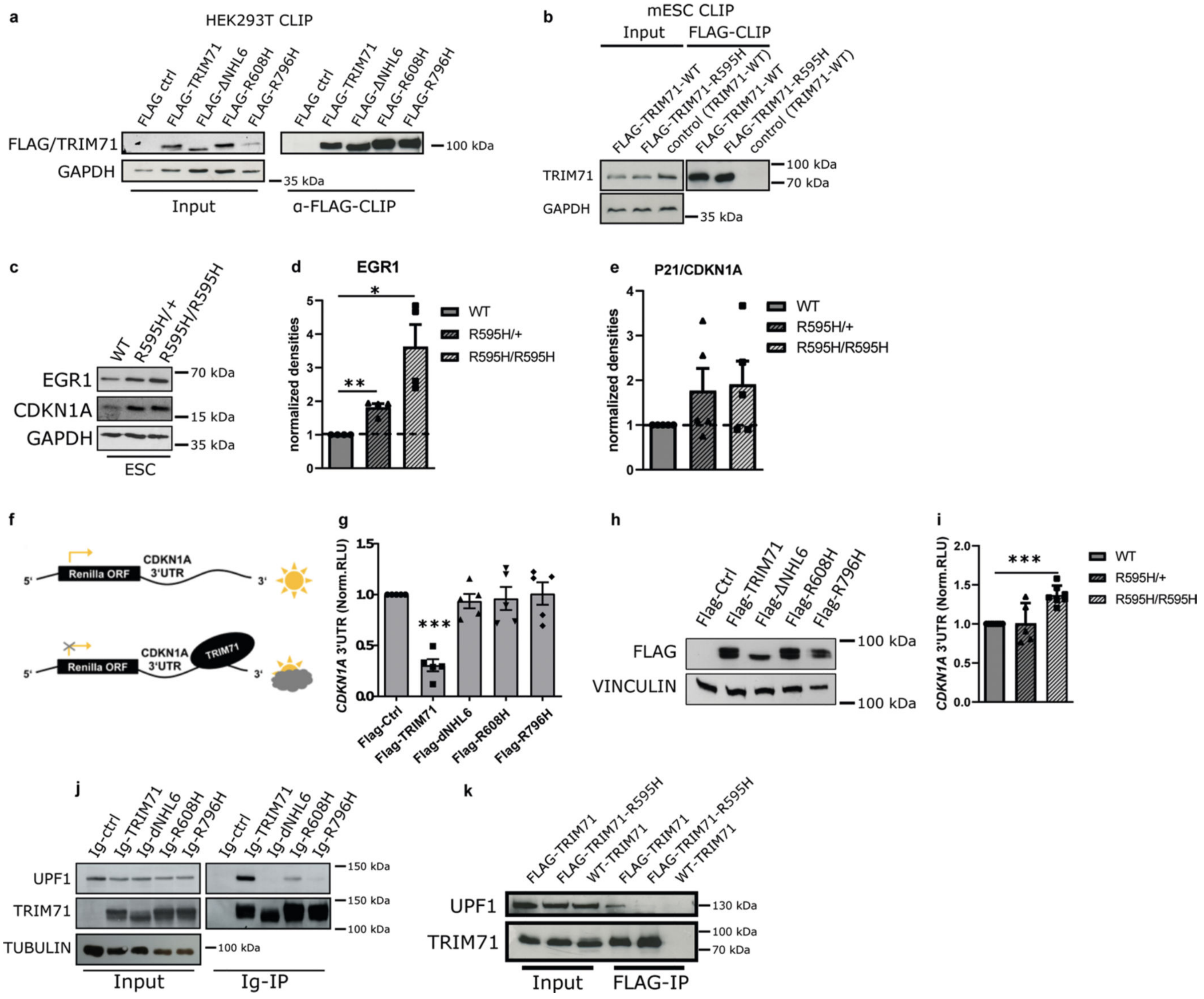

Extended Data Fig. 10 |. TRIM71 CH-mutations lead to deregulation of Cdkn1a/p21 and Egr1 and loss of interaction to the NMD factor UPF1.

a,b) Representative immunoblots for the CLIP-qPCR assays in a) HEK293T cells and b) mESC. c-e) Protein levels of EGR1 and P21/CDKN1A in WT and mutant TRIM71 mESC. c) Representative immunoblots showing protein levels of EGR1 and P21/CDKN1A. d,e) Quantitation of EGR1 (d) and P21/CDKN1A (e) protein levels from immunoblots in (c). f-i) De-repression of *CDKN1A* 3′UTR in HEK293T cells overexpressing TRIM71 mutants and in *Trim71* mutant mESCs. f) Schematic of luciferase assay to examine RNA target silencing by TRIM71 (CDKN1A as example). g) Luciferase reporter assay for the *CDKN1A* 3′UTR showing repression ability of the indicated TRIM71 constructs in HEK293T cells. Norm. RLU = normalized relative light units. h) Representative immunoblot showing TRIM71 construct overexpression for the CDKN1A-3′UTR luciferase assays in (g). i) Luciferase reporter assay for the *CDKN1A* 3′UTR showing repression ability of the indicated mESC line. j,k) CH-causing mutations impair TRIM71 binding to the NMD factor UPF1. Immunoblots show UPF1 enrichment upon co-precipitation with j) different

Ig-tagged TRIM71 constructs transfected into HEK293T cells, namely Ig-Ctrl, Ig-TRIM71, Ig-ΔNHL6, Ig-R608H, and Ig-R796H or k) with endogenous FLAG-tagged TRIM71 and TRIM71-R595H in mESC. Statistical significance was tested by a two-sided, one-sample t-test (d, e, g, i): *: $P<0.05$, **: $P<0.01$, ***: $P<0.001$. Data represented as mean±s.e.m., overlaid with individual data points. For detailed statistical information (d, e, g, i), see Supplementary Table 13. Source data are provided.

Supplementary Material

Refer to Web version on PubMed Central for supplementary material.

Authors

Phan Q. Duy[1,2,3,34], Stefan C. Weise[4,34], Claudia Marini[5], Xiao-Jun Li[6,7], Dan Liang[1], Peter J. Dahl[8,9], Shaojie Ma[1], Ana Spajic[1], Weilai Dong[10], Jane Juusola[11], Emre Kiziltug[2], Adam J. Kundishora[2], Sunil Koundal[12], Maysam Z. Pedram[12], Lucia A. Torres-Fernández[4], Kristian Händler[13,14,15], Elena De Domenico[13,14,15], Matthias Becker[13,14,15], Thomas Ulas[13,14,15], Stefan A. Juranek[16], Elisa Cuevas[17], Le Thi Hao[2], Bettina Jux[4], André M. M. Sousa[1], Fuchen Liu[1], Suel-Kee Kim[1], Mingfeng Li[1], Yiying Yang[18], Yutaka Takeo[2], Alvaro Duque[1], Carol Nelson-Williams[19], Yonghyun Ha[20], Kartiga Selvaganesan[20], Stephanie M. Robert[2], Amrita K. Singh[2], Garrett Allington[2], Charuta G. Furey[2], Andrew T. Timberlake[19], Benjamin C. Reeves[2], Hannah Smith[2], Ashley Dunbar[2], Tyrone DeSpenza Jr.[2], June Goto[21], Arnaud Marlier[2], Andres Moreno-De-Luca[22], Xin Yu[23], William E. Butler[23], Bob S. Carter[23], Evelyn M. R. Lake[20], R. Todd Constable[20], Pasko Rakic[1], Haifan Lin[18], Engin Deniz[24], Helene Benveniste[12], Nikhil S. Malvankar[8,9], Juvianee I. Estrada-Veras[25,26,27], Christopher A. Walsh[28,29,30], Seth L. Alper[30,31], Joachim L. Schultze[13,14,15], Katrin Paeschke[16], Angelika Doetzlhofer[6,7], F. Gregory Wulczyn[5], Sheng Chih Jin[32], Richard P. Lifton[10], Nenad Sestan[1], Waldemar Kolanus[4], Kristopher T. Kahle[23,28,30,33]

Affiliations

[1]Department of Neuroscience and Kavli Institute for Neuroscience, Yale University School of Medicine, New Haven, CT, USA.

[2]Department of Neurosurgery, Yale University School of Medicine, New Haven, CT, USA.

[3]Medical Scientist Training Program, Yale University School of Medicine, New Haven, CT, USA.

[4]Molecular Immunology and Cell Biology, Life & Medical Sciences Institute (LIMES), University of Bonn, Bonn, Germany.

[5]Institute for Cell Biology and Neurobiology, Charité-Universitätsmedizin Berlin, Corporate Member of Freie Universität Berlin, Humboldt-Universität zu Berlin, and Berlin Institute of Health, Berlin, Germany.

[6]Solomon H. Snyder Department of Neuroscience, Johns Hopkins University School of Medicine, Baltimore, MD, USA.

[7]Center for Hearing and Balance, Department of Otolaryngology-Head and Neck Surgery, Johns Hopkins University School of Medicine, Baltimore, MD, USA.

[8]Microbial Sciences Institute, Yale University, West Haven, CT, USA.

[9]Department of Molecular Biophysics and Biochemistry, Yale University, New Haven, CT, USA.

[10]Laboratory of Human Genetics and Genomics, The Rockefeller University, New York, NY, USA.

[11]GeneDx, Gaithersburg, MD, USA.

[12]Department of Anesthesiology, Yale University School of Medicine, New Haven, CT, USA.

[13]Systems Medicine, Deutsches Zentrum für Neurodegenerative Erkrankungen (DZNE), Bonn, Germany.

[14]Genomics and Immunoregulation, Life & Medical Sciences (LIMES) Institute, University of Bonn, Bonn, Germany.

[15]Deutsches Zentrum für Neurodegenerative Erkrankungen (DZNE). PRECISE Platform for Genomics and Epigenomics at DZNE and University of Bonn, Bonn, Germany.

[16]Department of Oncology, Hematology and Rheumatology, University Hospital Bonn, Bonn, Germany.

[17]Stem Cells and Regenerative Medicine Section, University College London Great Ormond Street Institute of Child Health, London, UK.

[18]Yale Stem Cell Center, Yale University School of Medicine, New Haven, CT, USA.

[19]Department of Genetics, Yale University School of Medicine, New Haven, CT, USA.

[20]Department of Radiology and Biomedical Imaging, Yale University School of Medicine, New Haven, CT, USA.

[21]Division of Pediatric Neurosurgery, Cincinnati Children's Hospital Medical Center, Cincinnati, OH, USA.

[22]Department of Radiology, Autism & Developmental Medicine Institute, Genomic Medicine Institute, Geisinger, Danville, PA, USA.

[23]Department of Neurosurgery, Massachusetts General Hospital, Harvard Medical School, Boston, MA, USA.

[24]Department of Pediatrics, Yale University School of Medicine, New Haven, CT, USA.

[25]Henry M. Jackson Foundation for the Advancement of Military Medicine, Bethesda, MD, USA.

[26]Pediatric Subspecialty Genetics Walter Reed National Military Medical Center, Bethesda, MD, USA.

[27]Murtha Cancer Center/Research Program, Department of Surgery, Uniformed Services University of the Health Sciences, Bethesda, MD, USA.

[28]Division of Genetics and Genomics, Manton Center for Orphan Disease Research, Department of Pediatrics, and Howard Hughes Medical Institute, Boston Children’s Hospital, Boston, MA, USA.

[29]Departments of Pediatrics and Neurology, Harvard Medical School, Boston, MA, USA.

[30]Broad Institute of MIT and Harvard, Cambridge, MA, USA.

[31]Division of Nephrology and Vascular Biology Research Center, Beth Israel Deaconess Medical Center and Department of Medicine, Harvard Medical School, Boston, MA, USA.

[32]Department of Genetics, Washington University School of Medicine, St. Louis, MO, USA.

[33]Harvard Center for Hydrocephalus and Neurodevelopmental Disorders, Massachusetts General Hospital, Boston, MA, USA.

[34]These authors contributed equally: Phan Q. Duy, Stefan C. Weise.

Acknowledgements

This work was supported by T32GM136651 (to P.Q.D.), F30HD106694 (to P.Q.D.), RO1NS111029 (to K.T.K.), David M. Rubenstein Fund for Hearing Research (to A. Doetzlhofer), 1R21NS121642-01 (to X.Y.), 1R01NS122904-01 (to X.Y.), the Rudi Schulte Institute (to K.T.K.), the Hydrocephalus Association Innovator Award (to K.T.K., E.D. and S.J.C.), 5R21NS116484-02 (to E.D.), National Institutes of Health (NIH)/National Heart, Lung, and Blood Institute (NHLBI) Pathway to Independence award R00HL143036-02 (to S.J.C.), Clinical & Translational Research Funding Program award CTSA1405 (to S.J.C.), Children’s Discovery Institute Faculty Scholar award CDI-FR-2021-926 (to S.J.C.), NIH Director’s New Innovator award 1DP2AI138259-01 (to N.S.M.), the Career Award at the Scientific Interfaces from Burroughs Welcome Fund (to N.S.M.), the Hartwell Foundation Individual Biomedical Research Award (to N.S.M.), MacBrainResource NIH MH113257 (to A. Duque), NIH DA023999 (to P.R.) and Deutsche Forschungsgemeinschaft (German Research Foundation) award WU 563/3-1 (to F.G.W.). W.K. is funded by the Deutsche Forschungsgemeinschaft under Germany’s Excellence Strategy EXC2151-390873048. All mechanical measurements were performed at the Yale West Campus Imaging Core. CSF outflow imaging was performed using the small animal imaging facility of the Center for Precision Cancer Modeling, sponsored by the Yale Cancer Center. The funders had no role in study design, data collection and analysis, decision to publish or preparation of the manuscript. Certain cartoons and diagrams were generated using BioRender.

Data availability

Unprocessed scans of all immunoblots in the paper are included as Source Data Fig. 1. WES data have been deposited in the database of Genotypes and Phenotypes under accession number phs000744. A Life Sciences Reporting Summary is available for this paper. In-house pipelines are available from the corresponding author upon reasonable request. Bulk

RNA sequencing data of mESCs have been deposited at the Gene Expression Omnibus under accession number GSE189420. Source data are provided with this paper.

References

1. Aristotle. The History of Animals http://classics.mit.edu/Aristotle/history_anim.mb.txt
2. Duy PQ et al. Brain ventricles as windows into brain development and disease. Neuron 110, 12–15 (2022). [PubMed: 34990576]
3. Persson EK, Hagberg G. & Uvebrant P. Disabilities in children with hydrocephalus—a population-based study of children aged between four and twelve years. Neuropediatrics 37, 330–336 (2006). [PubMed: 17357034]
4. Tully HM & Dobyns WB Infantile hydrocephalus: a review of epidemiology, classification and causes. Eur. J. Med. Genet 57, 359–368 (2014). [PubMed: 24932902]
5. Greenberg MS Handbook of Neurosurgery, 9th edition (Thieme, 2019).
6. Furey CG et al. De novo mutation in genes regulating neural stem cell fate in human congenital hydrocephalus. Neuron 99, 302–314 (2018). [PubMed: 29983323]
7. Jin SC et al. Exome sequencing implicates genetic disruption of prenatal neuro-gliogenesis in sporadic congenital hydrocephalus. Nat. Med 26, 1754–1765 (2020). [PubMed: 33077954]
8. Kousi M. & Katsanis N. The genetic basis of hydrocephalus. Annu. Rev. Neurosci 39, 409–435 (2016). [PubMed: 27145913]
9. Huang JK et al. Systematic evaluation of molecular networks for discovery of disease genes. Cell Syst. 6, 484–495 (2018). [PubMed: 29605183]
10. Willsey HR et al. Parallel in vivo analysis of large-effect autism genes implicates cortical neurogenesis and estrogen in risk and resilience. Neuron 109, 788–804 (2021). [PubMed: 33497602]
11. Kang HJ et al. Spatio-temporal transcriptome of the human brain. Nature 478, 483–489 (2011). [PubMed: 22031440]
12. Li M\. et al. Integrative functional genomic analysis of human brain development and neuropsychiatric risks. Science 362, eaat7615 (2018).
13. Miller JA et al. Transcriptional landscape of the prenatal human brain. Nature 508, 199–206 (2014). [PubMed: 24695229]
14. Nowakowski TJ et al. Spatiotemporal gene expression trajectories reveal developmental hierarchies of the human cortex. Science 358, 1318–1323 (2017). [PubMed: 29217575]
15. Willsey AJ et al. Coexpression networks implicate human midfetal deep cortical projection neurons in the pathogenesis of autism. Cell 155, 997–1007 (2013). [PubMed: 24267886]
16. Silbereis JC, Pochareddy S, Zhu Y, Li M. & Sestan N. The cellular and molecular landscapes of the developing human central nervous system. Neuron 89, 248–268 (2016). [PubMed: 26796689]
17. Mizrak D. et al. Single-cell analysis of regional differences in adult V-SVZ neural stem cell lineages. Cell Rep. 26, 394–406 (2019). [PubMed: 30625322]
18. DeSisto J. et al. Single-cell transcriptomic analyses of the developing meninges reveal meningeal fibroblast diversity and function. Dev. Cell 54, 43–59 (2020). [PubMed: 32634398]
19. Parikshak NN et al. Integrative functional genomic analyses implicate specific molecular pathways and circuits in autism. Cell 155, 1008–1021 (2013). [PubMed: 24267887]
20. Lancaster MA et al. Cerebral organoids model human brain development and microcephaly. Nature 501, 373–379 (2013). [PubMed: 23995685]
21. Duy PQ, Furey CG & Kahle KT *Trim71/lin-41* links an ancient miRNA pathway to human congenital hydrocephalus. Trends Mol. Med 25, 467–469 (2019). [PubMed: 30975633]
22. Spassky N. et al. Adult ependymal cells are postmitotic and are derived from radial glial cells during embryogenesis. J. Neurosci 25, 10–18 (2005). [PubMed: 15634762]
23. Coletti AM et al. Characterization of the ventricular-subventricular stem cell niche during human brain development. Development 145, dev170100 (2018).

24. Maller Schulman BR et al. The *let-7* microRNA target gene, *Mlin41/Trim71* is required for mouse embryonic survival and neural tube closure. Cell Cycle 7, 3935–3942 (2008). [PubMed: 19098426]
25. Chen J, Lai F. & Niswander L. The ubiquitin ligase *mLin41* temporally promotes neural progenitor cell maintenance through FGF signaling. Genes Dev. 26, 803–815 (2012). [PubMed: 22508726]
26. Mitschka S. et al. Co-existence of intact stemness and priming of neural differentiation programs in mES cells lacking Trim71. Sci. Rep 5, 11126 (2015). [PubMed: 26057209]
27. Nguyen DTT et al. The ubiquitin ligase LIN41/TRIM71 targets p53 to antagonize cell death and differentiation pathways during stem cell differentiation. Cell Death Differ. 24, 1063–1078 (2017). [PubMed: 28430184]
28. Dong J. et al. Single-cell RNA-seq analysis unveils a prevalent epithelial/mesenchymal hybrid state during mouse organogenesis. Genome Biol. 19, 31 (2018). [PubMed: 29540203]
29. Burke EE et al. Dissecting transcriptomic signatures of neuronal differentiation and maturation using iPSCs. Nat. Commun 11, 462 (2020). [PubMed: 31974374]
30. Onorati M. et al. Zika virus disrupts phospho-TBK1 localization and mitosis in human neuroepithelial stem cells and radial glia. Cell Rep. 16, 2576–2592 (2016). [PubMed: 27568284]
31. Dubois NC, Hofmann D, Kaloulis K, Bishop JM & Trumpp A. Nestin-Cre transgenic mouse line Nes-Cre1 mediates highly efficient Cre/loxP mediated recombination in the nervous system, kidney, and somite-derived tissues. Genesis 44, 355–360 (2006). [PubMed: 16847871]
32. Gorski JA et al. Cortical excitatory neurons and glia, but not GABAergic neurons, are produced in the Emx1-expressing lineage. J. Neurosci 22, 6309–6314 (2002). [PubMed: 12151506]
33. Worringer KA et al. The *let-7*/LIN-41 pathway regulates reprogramming to human induced pluripotent stem cells by controlling expression of prodifferentiation genes. Cell Stem Cell 14, 40–52 (2014). [PubMed: 24239284]
34. Newman AM et al. Robust enumeration of cell subsets from tissue expression profiles. Nat. Methods 12, 453–457 (2015). [PubMed: 25822800]
35. Steffensen AB et al. Cotransporter-mediated water transport underlying cerebrospinal fluid formation. Nat. Commun 9, 2167 (2018). [PubMed: 29867199]
36. Karimy JK et al. Inflammation-dependent cerebrospinal fluid hypersecretion by the choroid plexus epithelium in posthemorrhagic hydrocephalus. Nat. Med 23, 997–1003 (2017). [PubMed: 28692063]
37. Date P. et al. Visualizing flow in an intact CSF network using optical coherence tomography: implications for human congenital hydrocephalus. Sci. Rep 9, 6196 (2019). [PubMed: 30996265]
38. Roossien DH, Miller KE & Gallo G. Ciliobrevins as tools for studying dynein motor function. Front. Cell Neurosci 9, 252 (2015). [PubMed: 26217180]
39. Peña A, Harris NG, Bolton MD, Czosnyka M. & Pickard JD Communicating hydrocephalus: the biomechanics of progressive ventricular enlargement revisited. Acta Neurochir. Suppl 81, 59–63 (2002). [PubMed: 12168357]
40. Duy PQ & Kahle KT Intraventricular cerebrospinal fluid turbulence in pediatric communicating hydrocephalus. Neurology 97, 246–247 (2021). [PubMed: 34031199]
41. Elkin BS, Ilankovan A. & Morrison B. Age-dependent regional mechanical properties of the rat hippocampus and cortex. J. Biomech. Eng 132, 011010 (2010). [PubMed: 20524748]
42. Canovic EP et al. Characterizing multiscale mechanical properties of brain tissue using atomic force microscopy, impact indentation, and rheometry. J. Vis. Exp 54201 (2016).
43. Yalcin SE et al. Electric field stimulates production of highly conductive microbial OmcZ nanowires. Nat. Chem. Biol 16, 1136–1142 (2020). [PubMed: 32807967]
44. Torres-Fernández LA et al. The mRNA repressor TRIM71 cooperates with nonsense-mediated decay factors to destabilize the mRNA of CDKN1A/p21. Nucleic Acids Res. 47, 11861–11879 (2019). [PubMed: 31732746]
45. Hafner M. et al. Transcriptome-wide identification of RNA-binding protein and microRNA target sites by PAR-CLIP. Cell 141, 129–141 (2010). [PubMed: 20371350]
46. Chang H-MM et al. Trim71 cooperates with microRNAs to repress Cdkn1a expression and promote embryonic stem cell proliferation. Nat. Commun 3, 923 (2012). [PubMed: 22735451]

47. Welte T. et al. The RNA hairpin binder TRIM71 modulates alternative splicing by repressing MBNL1. Genes Dev. 33, 1221–1235 (2019). [PubMed: 31371437]

48. Phoenix TN & Temple S. Spred1, a negative regulator of Ras-MAPK-ERK, is enriched in CNS germinal zones, dampens NSC proliferation, and maintains ventricular zone structure. Genes Dev. 24, 45–56 (2010). [PubMed: 20047999]

49. DeSpenza T. et al. PTEN mutations in autism spectrum disorder and congenital hydrocephalus: developmental pleiotropy and therapeutic targets. Trends Neurosci. 44, 961–976 (2021). [PubMed: 34625286]

50. van der Linden V. et al. Association of severe hydrocephalus with congenital Zika syndrome. JAMA Neurol. 76, 203 (2019). [PubMed: 30452526]

51. Su J. et al. Novel compound heterozygous frameshift variants in *WDR81* associated with congenital hydrocephalus 3 with brain anomalies: first Chinese prenatal case confirms *WDR81* involvement. Mol. Genet. Genom. Med 9, e1624 (2021).

52. Cavallin M. et al. *WDR81* mutations cause extreme microcephaly and impair mitotic progression in human fibroblasts and *Drosophila* neural stem cells. Brain 140, 2597–2609 (2017). [PubMed: 28969387]

53. Sullivan W. et al. Exome sequencing as a potential diagnostic adjunct in sporadic congenital hydrocephalus. JAMA Pediatr. 175, 310 (2021). [PubMed: 33196764]

54. Rakic P. Evolution of the neocortex: a perspective from developmental biology. Nat. Rev. Neurosci 10, 724–735 (2009). [PubMed: 19763105]

55. Duran D. et al. Mutations in chromatin modifier and ephrin signaling genes in vein of Galen malformation. Neuron 101, 429–443 (2019). [PubMed: 30578106]

56. McKenna A. et al. The Genome Analysis Toolkit: a MapReduce framework for analyzing next-generation DNA sequencing data. Genome Res. 20, 1297–1303 (2010). [PubMed: 20644199]

57. Van der Auwera GA et al. From FastQ data to high confidence variant calls: the Genome Analysis Toolkit best practices pipeline. Curr. Protoc. Bioinforma 43, 11.10.1–11.10.33 (2013).

58. Garrison E. & Marth G. Haplotype-based variant detection from short-read sequencing. Preprint at https://arxiv.org/abs/1207.3907 (2012).

59. Lek M. et al. Analysis of protein-coding genetic variation in 60,706 humans. Nature 536, 285–291 (2016). [PubMed: 27535533]

60. Gudmundsson S. et al. Addendum: the mutational constraint spectrum quantified from variation in 141,456 humans. Nature 597, E3–E4 (2021). [PubMed: 34373650]

61. Taliun D. et al. Sequencing of 53,831 diverse genomes from the NHLBI TOPMed Program. Nature 590, 290–299 (2021). [PubMed: 33568819]

62. Samocha KE et al. Regional missense constraint improves variant deleteriousness prediction. Preprint at https://www.biorxiv.org/content/10.1101/148353v1 (2017).

63. Dong C. et al. Comparison and integration of deleteriousness prediction methods for nonsynonymous SNVs in whole exome sequencing studies. Hum. Mol. Genet 24, 2125–2137 (2015). [PubMed: 25552646]

64. Wei Q. et al. A Bayesian framework for de novo mutation calling in parents–offspring trios. Bioinformatics 31, 1375–1381 (2015). [PubMed: 25535243]

65. Jin SC et al. Contribution of rare inherited and de novo variants in 2,871 congenital heart disease probands. Nat. Genet 49, 1593–1601 (2017). [PubMed: 28991257]

66. Robinson JT, Thorvaldsdóttir H, Wenger AM, Zehir A. & Mesirov JP Variant review with the Integrative Genomics Viewer. Cancer Res. 77, e31–e34 (2017). [PubMed: 29092934]

67. Price AL et al. Principal components analysis corrects for stratification in genome-wide association studies. Nat. Genet 38, 904–909 (2006). [PubMed: 16862161]

68. Ware JS, Samocha KE, Homsy J. & Daly MJ Interpreting de novo variation in human disease using denovolyzeR. Curr. Protoc. Hum. Genet 87, 7.25.1–7.25.15 (2015).

69. Jin SC et al. Mutations disrupting neuritogenesis genes confer risk for cerebral palsy. Nat. Genet 52, 1046–1056 (2020). [PubMed: 32989326]

70. Piñero J. et al. DisGeNET: a comprehensive platform integrating information on human disease-associated genes and variants. Nucleic Acids Res. 45, D833–D839 (2017). [PubMed: 27924018]

71. Zhang B. & Horvath S. A general framework for weighted gene co-expression network analysis. Stat. Appl. Genet. Mol. Biol 4, Article17 (2005).
72. Walker RL et al. Genetic control of expression and splicing in developing human brain informs disease mechanisms. Cell 179, 750–771 (2019). [PubMed: 31626773]
73. Yang H, Wang H. & Jaenisch R. Generating genetically modified mice using CRISPR/Cas-mediated genome engineering. Nat. Protoc 9, 1956–1968 (2014). [PubMed: 25058643]
74. Chen S, Lee B, Lee AY-F, Modzelewski AJ & He L. Highly efficient mouse genome editing by CRISPR ribonucleoprotein electroporation of zygotes. J. Biol. Chem 291, 14457–14467 (2016). [PubMed: 27151215]
75. Behringer R, Gertsenstein M, Nagy KV & Nagy A. Manipulating the Mouse Embryo: A Laboratory Manual (Cold Spring Harbor Laboratory Press, 2014).
76. Nichols J. & Jones K. Derivation of mouse embryonic stem (ES) cell lines using small-molecule inhibitors of Erk and Gsk3 signaling (2i). Cold Spring Harb. Protoc 10.1101/pdb.prot094086 (2017).
77. Sbalzarini IF & Koumoutsakos P. Feature point tracking and trajectory analysis for video imaging in cell biology. J. Struct. Biol 151, 182–195 (2005). [PubMed: 16043363]
78. Chenouard N. et al. Objective comparison of particle tracking methods. Nat. Methods 11, 281–289 (2014). [PubMed: 24441936]
79. Ran FA et al. Genome engineering using the CRISPR–Cas9 system. Nat. Protoc 8, 2281–2308 (2013). [PubMed: 24157548]
80. Benhalevy D, McFarland HL, Sarshad AA & Hafner M. PAR-CLIP and streamlined small RNA cDNA library preparation protocol for the identification of RNA binding protein target sites. Methods 118–119, 41–49 (2017).

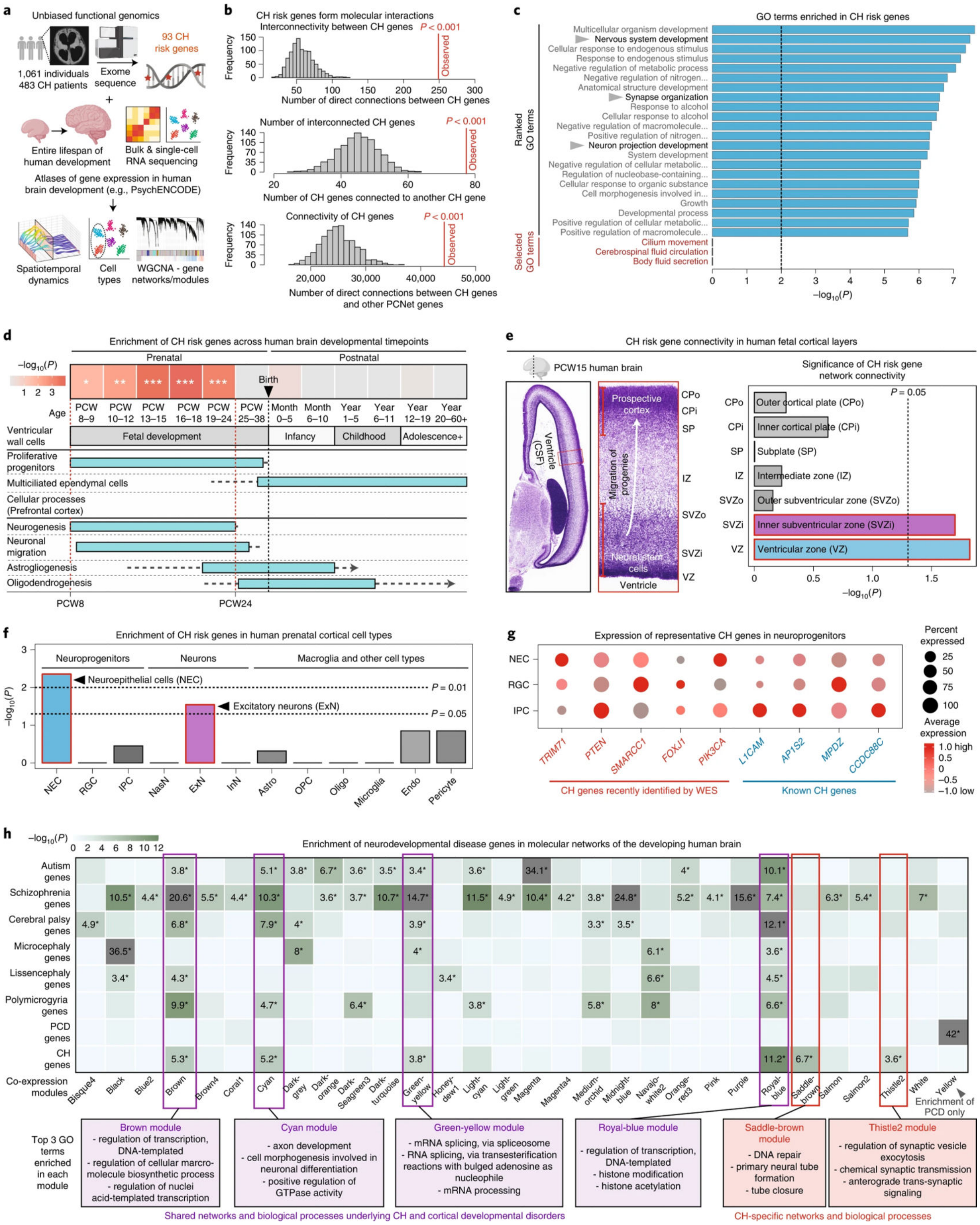

Fig. 1 |. Convergence of CH genetic risk in discrete gene networks and cell types during human brain development.

a, Overview of functional genomics analyses. See Supplementary Table 3 for published transcriptomic datasets that were used for analyses. **b**, Number of direct PCNet interactions among CH risk genes (top), total number of CH risk genes that are connected to at least one other CH risk gene (middle) and number of interactions with CH risk genes and any other genes in PCNet (bottom). Red line indicates the observed value, and the gray histogram shows the null distribution of 1,000 permutations. Significance was calculated by permutation tests (Methods). $P = 0$ for all comparisons. **c**, GO analysis of CH risk genes, including ranked and selected terms. Significance was calculated by two-sided Fisher's exact test. **d**, Enrichment of CH risk genes across developmental time points of the human brain. Analyzed transcriptomic dataset from ref. [12]. Significance was calculated by comparing to background expression using one-sided Wilcoxon rank-sum test: $^{*}P < 0.05$, $^{**}P < 0.01$, $^{***}P < 0.001$ and NS (not significant): $P > 0.05$. Cellular processes were based on ref. [16] and ref. [23]. **e**, Significance of connectivity on BrainSpan layer-specific CH risk gene networks. Analyzed transcriptomic dataset from ref. [13]. Fetal brain image was from the BrainSpan atlas. Significance was calculated by permutation tests (Methods). **f**, Enrichment of CH risk genes in prenatal human brain cell types. Analyzed transcriptomic dataset from ref. [12]. RGC, radial glia cell; IPC, intermediate progenitor cell; NasN, nascent neuron; InN, inhibitory neuron; Astro, astrocyte; OPC, oligodendrocyte precursor cell; Oligo, oligodendrocyte; Endo, endothelial cell. Significance was calculated by hypergeometric test. **g**, Average scaled expression of representative CH genes in neuroprogenitor populations (NEC, RGC and IPC). Analyzed transcriptomic dataset from ref. [12]. **h**, Module-level enrichment for disease risk genes. Modules were constructed via WGCNA of BrainSpan data (Methods). Only modules demonstrating significant enrichment for tested gene sets are shown. Logistic regression for indicator-based enrichment was used to calculate P values. Tiles labeled with $-\log_{10}(P)$ and an asterisk represent statistically significant enrichment at the Bonferroni multiple testing cutoff ($\alpha = 0.05/88 = 5.68 \times 10^{-4}$).

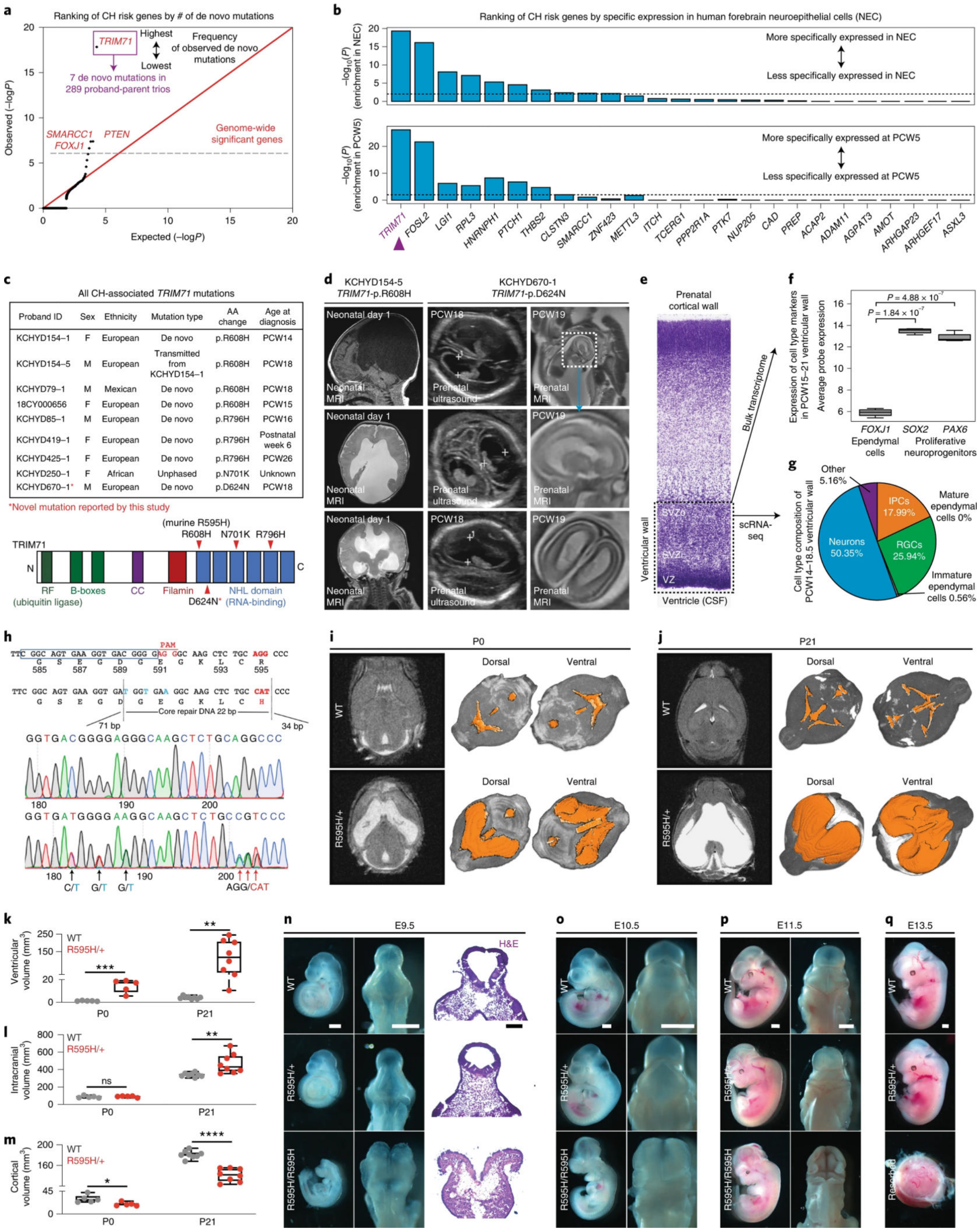

Proband ID	Sex	Ethnicity	Mutation type	AA change	Age at diagnosis
KCHYD154–1	F	European	De novo	p.R608H	PCW14
KCHYD154–5	M	European	Transmitted from KCHYD154–1	p.R608H	PCW18
KCHYD79–1	M	Mexican	De novo	p.R608H	PCW18
18CY000656	F	European	De novo	p.R608H	PCW15
KCHYD85–1	M	European	De novo	p.R796H	PCW16
KCHYD419–1	F	European	De novo	p.R796H	Postnatal week 6
KCHYD425–1	F	European	De novo	p.R796H	PCW26
KCHYD250–1	F	African	Unphased	p.N701K	Unknown
KCHYD670–1*	M	European	De novo	p.D624N	PCW18

*Novel mutation reported by this study

Fig. 2 |. A mouse model that harbors the murine homolog (R595H) of the human CH-associated missense mutation in *TRIM71* (R608H) exhibits ventriculomegaly and cortical hypoplasia.

a, Quantile–quantile plot of observed versus expected *P* values for DNMs in each gene in 289 cases. *P* values were calculated using a one-sided Poisson test (Methods). **b**, Ranking of CH risk genes by enrichment in human neuroepithelial cells (NEC) and at PCW5 based on the transcriptomic dataset from ref. [12]. Significance was calculated by two-sided Wilcoxon rank-sum test. **c**, *TRIM71* mutant patients with CH and mutations identified to date. The TRIM71 polypeptide domain schematic shows clustering of all mutations in the

RNA-binding NHL domain. **d**, Brain MRI or ultrasound imaging from *TRIM71* mutant patients with CH demonstrating ventriculomegaly phenotype. Prenatal imaging (ultrasound and MRI) is shown for patient KCHYD670–1. **e**–**g**, Expression analysis of published bulk data[13] (**f**) and single-cell transcriptomic data[14] (**g**) of the prenatal human brain ventricular wall (comprising VZ and SVZ) for cell-type-specific markers. Box plot (in **f**): median (line) and 25th and 75th percentiles (box); whiskers extend up to 1.5 times the interquartile range from the top (bottom) of the box to the furthest datum within that distance ($n = 4$ brains). Significance was calculated by two-sided unpaired t-test in **f**. IPC, intermediate progenitor cell; RGC, radial glia cell. **h**, Generation of $Trim71^{R595H}$ mutant mice by CRISPR–Cas9 (Methods). Sanger sequencing shows substitution of AGG with CAT, encoding a change from R^{595} to H^{595}. **i**, **j**, Brain MRI and 3D reconstructions of the ventricular system based on MRI scans of WT and hydrocephalic $Trim71^{R595H/+}$ mice at P0 and P21. **k**–**m**, Quantitation of ventricular volume (**k**), intracranial volume (**l**) and cortical volume (**m**) from MRI scans of hydrocephalic $Trim71^{R595H/+}$ mice compared to WT littermate controls at P0 and P21. Significance was tested by two-sided unpaired t-test (**k**–**m**): $*P < 0.05$, $**P < 0.01$, $***P < 0.001$, $****P < 0.0001$ and NS (not significant): $P > 0.05$. Data are represented as box plots: median (line) and 25th and 75th percentiles (box); whiskers go down to the smallest value and up to the largest, overlaid with individual data points. For detailed statistical information, see Supplementary Table 13. **n**–**q**, Exencephaly in $Trim71^{R595H/R595H}$ embryos. No homozygous *Trim71* mutants can be recovered by E13.5 with resorption of embryos. Scale bars, 500 μm.

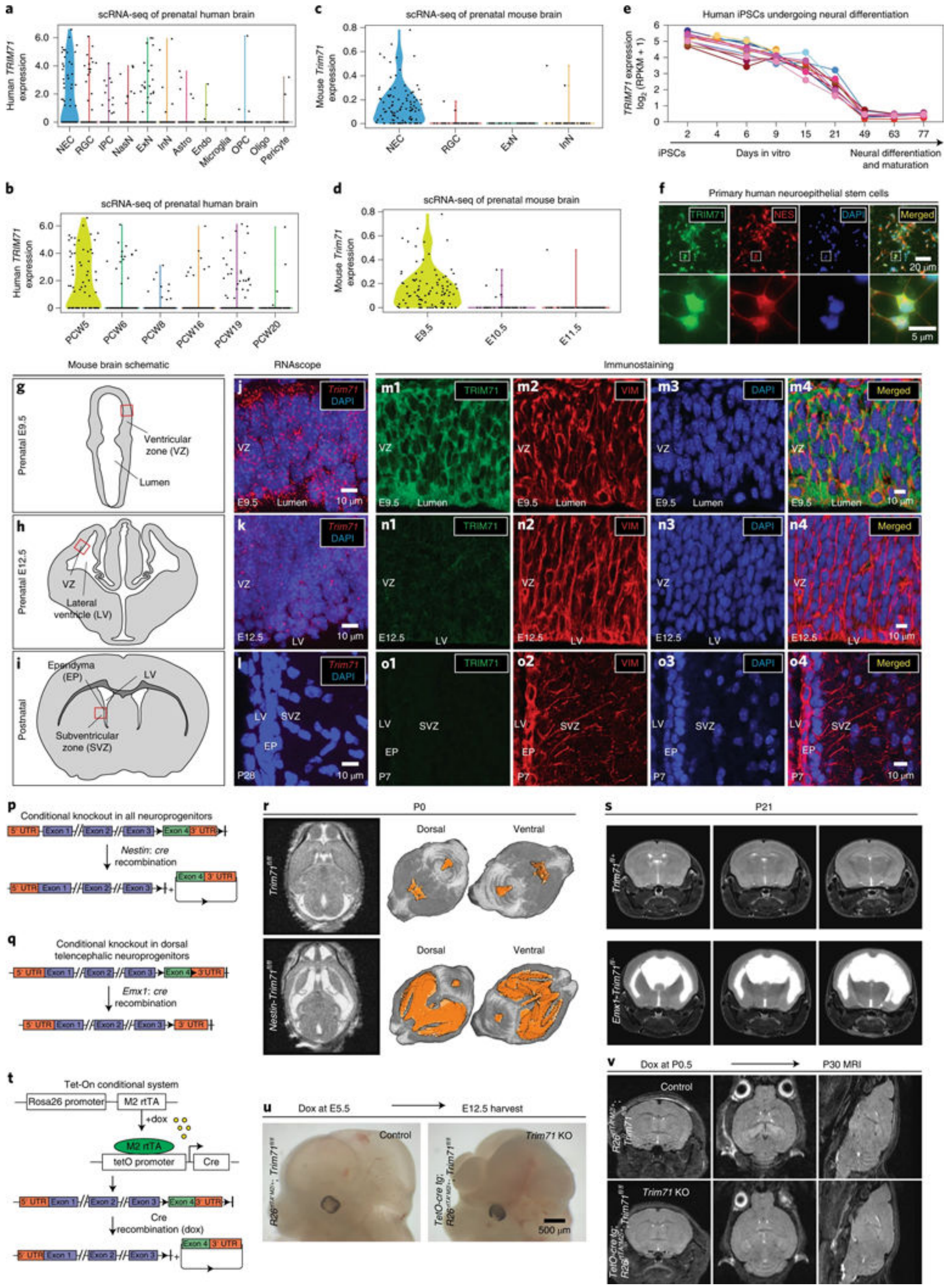

Fig. 3 |. TRIM71 is expressed in neuroepithelial cells and is required in embryonic neuroprogenitors for forebrain morphogenesis.

a, **b**, Violin plots showing *TRIM71* expression across time points and cell types during human brain development. Analyzed transcriptomic dataset from ref. [12]. NEC, neuroepithelial cell; RGC, radial glia cell; IPC, intermediate progenitor cell; NasN, nascent neuron; ExN, excitatory neuron; InN, inhibitory neuron; Astro, astrocyte; OPC, oligodendrocyte precursor cell; Oligo, oligodendrocyte; Endo, endothelial cell. **c**, **d**, Violin plots showing *Trim71* expression across time points and cell types during mouse brain development. Analyzed transcriptomic dataset from ref. [28]. **e**, *TRIM71* expression throughout the course of in vitro neural differentiation in human iPSCs. Analyzed transcriptomic dataset from ref. [29]. **f**, TRIM71 immunostaining in NES+ human primary neuroepithelial cells. **g–i**, Schematic of mouse brain tissue sections at different time points. Red squares indicate areas selected for imaging in **j–o**. **j–l**, RNAscope studies of *Trim71* mRNA expression in the WT mouse brain. Abundant *Trim71* expression was observed in the WT mouse neuroepithelium at E9.5 (**j**), with rapid reduction in levels by E12.5 (**k**). *Trim71* RNA was not detected in the P28 WT mouse ependyma (**l**). **m–o**, Immunostaining shows TRIM71 expression in VIM+ neuroepithelial cells in E9.5 WT mouse neuroepithelium (**m**), followed by rapid reduction thereafter with no detectable expression in E12.5 WT neuroepithelium (**n**) or in P7 WT mouse ependyma (**o**). **p**, Schematic of conditional *Trim71* allele[26] and Cre-mediated recombination to delete *Trim71* in all embryonic neuroprogenitors by *Nestin-Cre* driver. **q**, Schematic of novel conditional *Trim71* allele before and after Cre-mediated recombination leading to excision of exon 4, causing conditional KO of *Trim71* in neuroprogenitors fated for the dorsal telencephalon directed by *Emx1-Cre* driver. **r**, Brain MRI demonstrates severe ventriculomegaly at P0 in a representative hydrocephalic *Nestin-Cre;Trim71*$^{fl/fl}$ mouse compared to a *Trim71*$^{fl/fl}$ control. 3D reconstructions of the ventricular system based on MRI scans are shown. **s**, Brain MRI demonstrates ventriculomegaly at P21 in hydrocephalic *Emx1-Trim71*$^{fl/-}$ compared to a *Trim71*$^{fl/+}$ control. **t**, Schematic of Tet-On system to conditionally KO *Trim71* upon the administration of dox (Methods). **u**, Exencephaly in E12.5 *Trim71* KO (*TetO-cre tg;R26*$^{rtTA*M2/+}$*;Trim71*$^{fl/fl}$) embryos but not in control embryos (*R26*$^{rtTA*M2/+}$*;Trim71*$^{fl/fl}$) after dox administration at E5.5. **v**, Brain MRI of P30 *Trim71* KO (*TetO-cre tg;R26*$^{rtTA*M2/+}$*;Trim71*$^{fl/fl}$) and control (*R26*$^{rtTA*M2/+}$*;Trim71*$^{fl/fl}$) mice after dox administration at birth (P0.5).

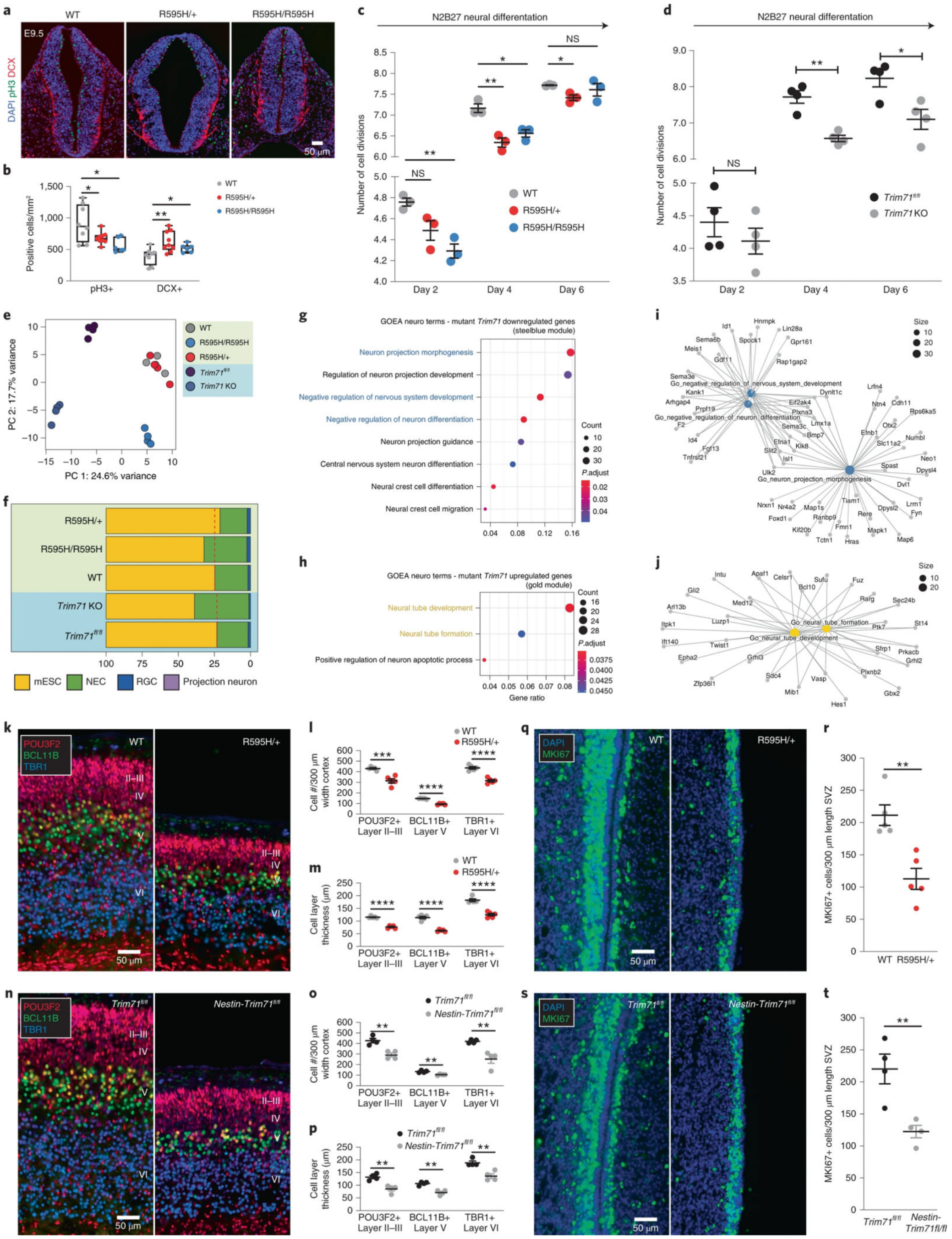

Fig. 4 |. Mutant TRIM71 alters neural stem cell progression, leading to premature differentiation with reduced proliferation.

a, Immunostaining of pH3 (marker of cell proliferation) cells and DCX (marker of immature neuroblasts) in the neuroepithelia of WT, *Trim71*$^{R595H/+}$ and *Trim71*$^{R595H/R595H}$ embryos at E9.5. **b**, Quantitation of pH3^{+} cells and DCX+ cells in the E9.5 neural tube neuroepithelia of WT, *Trim71*$^{R595H/+}$ and *Trim71*$^{R595H/R595H}$ embryos. **c**, **d**, WT and *Trim71* mutant mESC divisions upon neural differentiation. **e**, Principal component analysis of bulk RNA sequencing data from *Trim71*$^{fl/fl}$, *Trim71* KO, WT, *Trim71*$^{R595H/+}$ and *Trim71*$^{R595H/R595H}$

mESCs. *Trim71* KO and $Trim71^{R595H/R595H}$ replicates cluster with respect to their controls in PC2. $Trim71^{R595H/+}$ transcriptomes cluster together with their WT controls. Each point represents a replicate. **f**, CIBERSORT cell deconvolution with the RNA sequencing data over all genotypes shows a distinct shift from mESC to NEC pattern in $Trim71^{R595H/R595H}$ and *Trim71* KO mESCs compared to their respective controls. NEC, neuroepithelial cell; RGC, radial glia cell. **g**, **h**, Gene ontology enrichment analysis (GOEA) with neural-related terms of genes reduced (steelblue module) (**g**) or increased (gold module) (**h**) in *Trim71* KO and $Trim71^{R595H/R595H}$. *P* values were calculated by hypergeometric test with Benjamini–Hochberg correction. **i**, **j**, Gene networks of highlighted GO terms in **g** and **h** of genes reduced (**i**) or increased (**j**) in *Trim71* KO and $Trim71^{R595H/R595H}$ mESCs. **k**–**p**, Immunostaining of POU3F2/BRN2 (layer II–III cortical neurons), BCL11B/CTIP2 (layer V cortical neurons) and TBR1 (layer VI cortical neurons) in cortices of control (WT and $Trim71^{fl/fl}$) and hydrocephalic *Trim71* mutant mouse models ($Trim71^{R595H/+}$ and *Nestin-Cre;*$Trim71^{fl/fl}$) at P0 with associated cell counts and layer thickness. **q**–**t**, Immunostaining of MKI67 (marker of cell proliferation) in the SVZs of control (WT and $Trim71^{fl/fl}$) and hydrocephalic *Trim71* mutant mouse models ($Trim71^{R595H/+}$ and *Nestin-Cre;*$Trim71^{fl/fl}$) at P0 with associated cell counts. Statistical significance was tested by a two-sided unpaired t-test (**b**–**d**, **l**, **m**, **o**, **p**, **r**, **t**): $^{*}P < 0.05$, $^{**}P < 0.01$, $^{***}P < 0.001$, $^{****}P < 0.0001$ and NS (not significant): $P > 0.05$. Data are represented as a box plot (**b**): median (line) and 25th and 75th percentiles (box); whiskers go down to the smallest value and up to the largest. Data are represented as mean ± s.e.m. (**c**, **d**, **l**, **m**, **o**, **p**, **r**, **t**). Individual data points were overlaid. For detailed statistical information (**b**–**d**, **l**, **m**, **o**, **p**, **r**, **t**), see Supplementary Table 13.

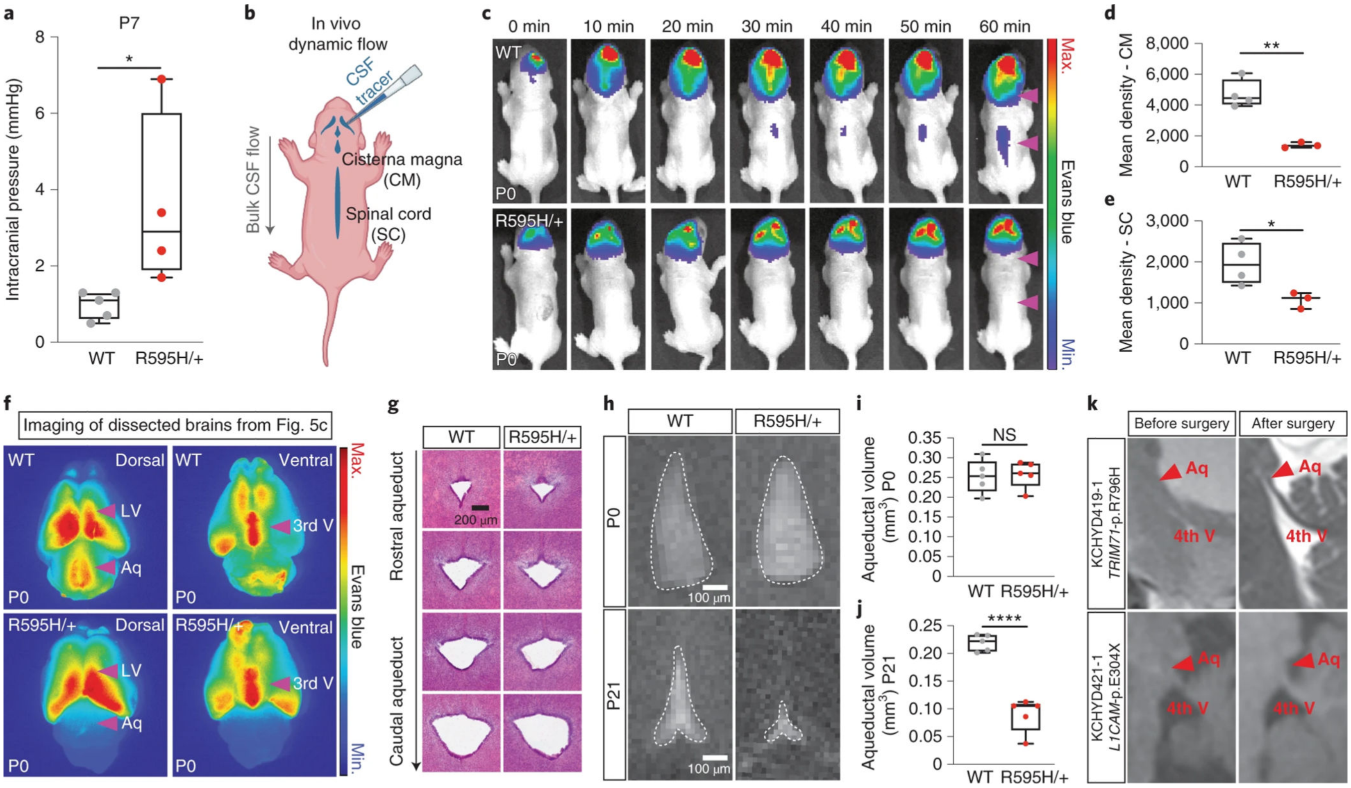

Fig. 5 |. Development of secondary aqueductal stenosis due to forebrain ventriculomegaly in hydrocephalic *Trim71$^{R595H/+}$* mice.

a, Measurement of ICP in P7 hydrocephalic *Trim71$^{R595H/+}$* mice and WT controls. **b**, Schematic of live imaging paradigm to characterize CSF outflow. A fluorescent CSF tracer (1% Evans blue) is injected into a lateral ventricle of a P0 mouse pup. The tracer diffuses throughout the entire ventricular system and then drains into the cisterna magna (CM) and spinal cord (SC). Tracer outflow from the ventricles is visualized by in vivo optical imaging. **c**, Images of pseudo-color fluorescence superimposed on a white light image from a P0 hydrocephalic *Trim71$^{R595H/+}$* mouse and a WT control at different time points (in minutes) after ventricular injection of 1% Evans blue. The purple arrowheads show CM and SC regions. **d**, **e**, Quantitation of fluorescence intensities (mean intensity) of Evans blue distribution to CM (**d**) or SC (**e**) 1 hour after ventricular dye injection in P0 hydrocephalic *Trim71$^{R595H/+}$* and WT control mice. **f**, Dorsal and ventral views of brains dissected from a P0 hydrocephalic *Trim71$^{R595H/+}$* mouse and a WT control 1 hour after ventricular injection of the CSF tracer. LV, lateral ventricle; 3rd V, third ventricle; Aq, cerebral aqueduct. **g**, H&E-stained images of histological sections throughout the rostrocaudal extent of the midbrain cerebral aqueduct in a P0 hydrocephalic *Trim71$^{R595H/+}$* mouse and a WT control. **h**, Representative images of the midbrain cerebral aqueduct from hydrocephalic *Trim71$^{R595H/+}$* mice and WT controls at P0 (top panels) and P21 (bottom panels). **i**, **j**, Quantitation of aqueduct volume from hydrocephalic *Trim71$^{R595H/+}$* mice and WT controls at P0 (**i**) and P21 (**j**). **k**, Brain MRI showing the cerebral aqueduct from a *TRIM71* mutant (top panels) or *L1CAM* mutant (bottom panels) patient with CH before and after neurosurgical CSF diversion. 4th V, fourth ventricle. Statistical significance was tested by a two-sided unpaired *t*-test (**a**, **d**, **e**, **i**, **j**): *$P < 0.05$, **$P < 0.01$, ****$P < 0.0001$ and NS (not significant): $P > 0.05$. Data are represented as box plots: median (line) and 25th and 75th percentiles (box); whiskers go down to the smallest value and up to the largest, overlaid with individual data points. For detailed statistical information (**a**, **d**, **e**, **i**, **j**), see Supplementary Table 13.

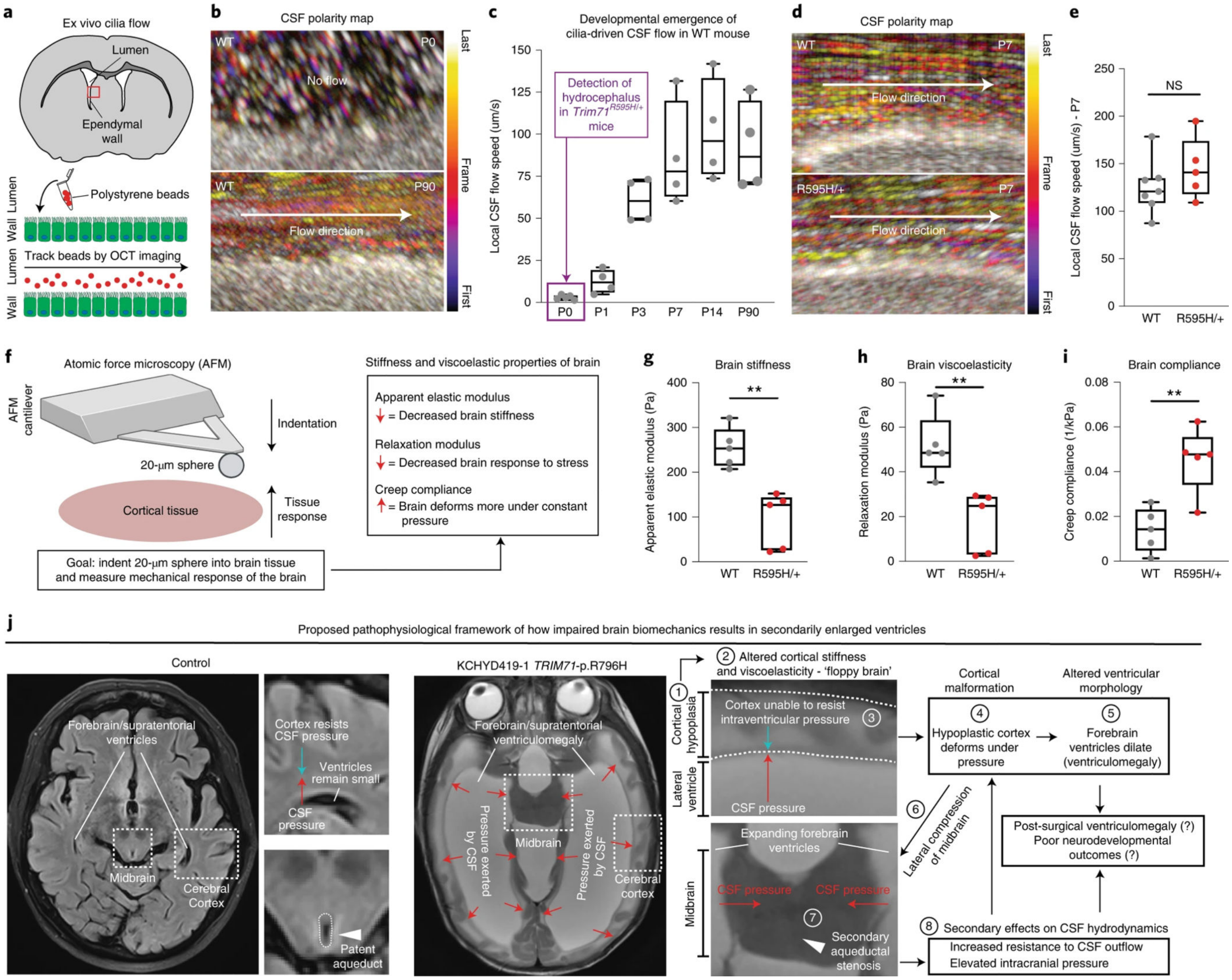

Fig. 6 |. Abnormal brain biomechanics facilitates secondary ventricular dilation in hydrocephalic *Trim71*$^{R595H/+}$ mice.

a, Schematic of assay to characterize cilia-driven CSF flow in mouse brain sections using OCT imaging. **b**, Representative flow polarity maps demonstrating bead trajectories (by temporal color coding) over time in WT mouse brain explants at P0 and at P21. Color bar represents color versus corresponding frame in the color-coded image. **c**, Quantitation of local CSF flow speeds at ventricular walls of WT mice at P0 (*n* = 5 mice), P1 (*n* = 4 mice), P3 (*n* = 4 mice), P7 (*n* = 4 mice), P14 (*n* = 4 mice) and P90 (*n* = 4 mice). **d**, Representative flow polarity maps demonstrating bead trajectories over time in mouse brain explants from a hydrocephalic *Trim71*$^{R595H/+}$ mouse and a WT control at P7. Color bar represents color versus corresponding frame in the color-coded image. **e**, Quantitation of local CSF flow speeds at ventricular walls of P7 hydrocephalic *Trim71*$^{R595H/+}$ mice and WT controls. **f**, Schematic of AFM indentation experiments to characterize biomechanics of brain tissue. A summary of findings from hydrocephalic *Trim71*$^{R595H/+}$ mice is shown in the box. **g**–**i**, Quantitation of brain stiffness (**g**), viscoelasticity (**h**) and compliance (**i**) in cortical tissues from P7 hydrocephalic *Trim71*$^{R595H/+}$ mice and WT controls. **j**, Proposed pathophysiological mechanism of ventriculomegaly due to impaired brain biomechanics in *TRIM71*-mutant CH. CSF normally generates a positive pressure in the ventricles that must be counteracted by the surrounding brain parenchyma. In the setting of cortical hypoplasia, altered brain biomechanics results in a floppy brain that is unable to resist the pressure exerted by CSF, facilitating secondary ventricular dilation in the absence of a primary defect in CSF. Continued expansion of the floppy brain parenchyma eventually compresses the midbrain, leading to secondary aqueductal stenosis. MRI of control adult human brain was obtained from OpenNeuro Dataset ds000221. Statistical significance was tested by a two-sided unpaired t-test (**e**, **g–i**): **$P < 0.01$ and NS (not significant): $P > 0.05$. Data are represented as box plots: median (line) and 25th and 75th percentiles (box); whiskers go down to the smallest value and up to the largest, overlaid with individual data points. For detailed statistical information (**e**, **g–i**), see Supplementary Table 13.

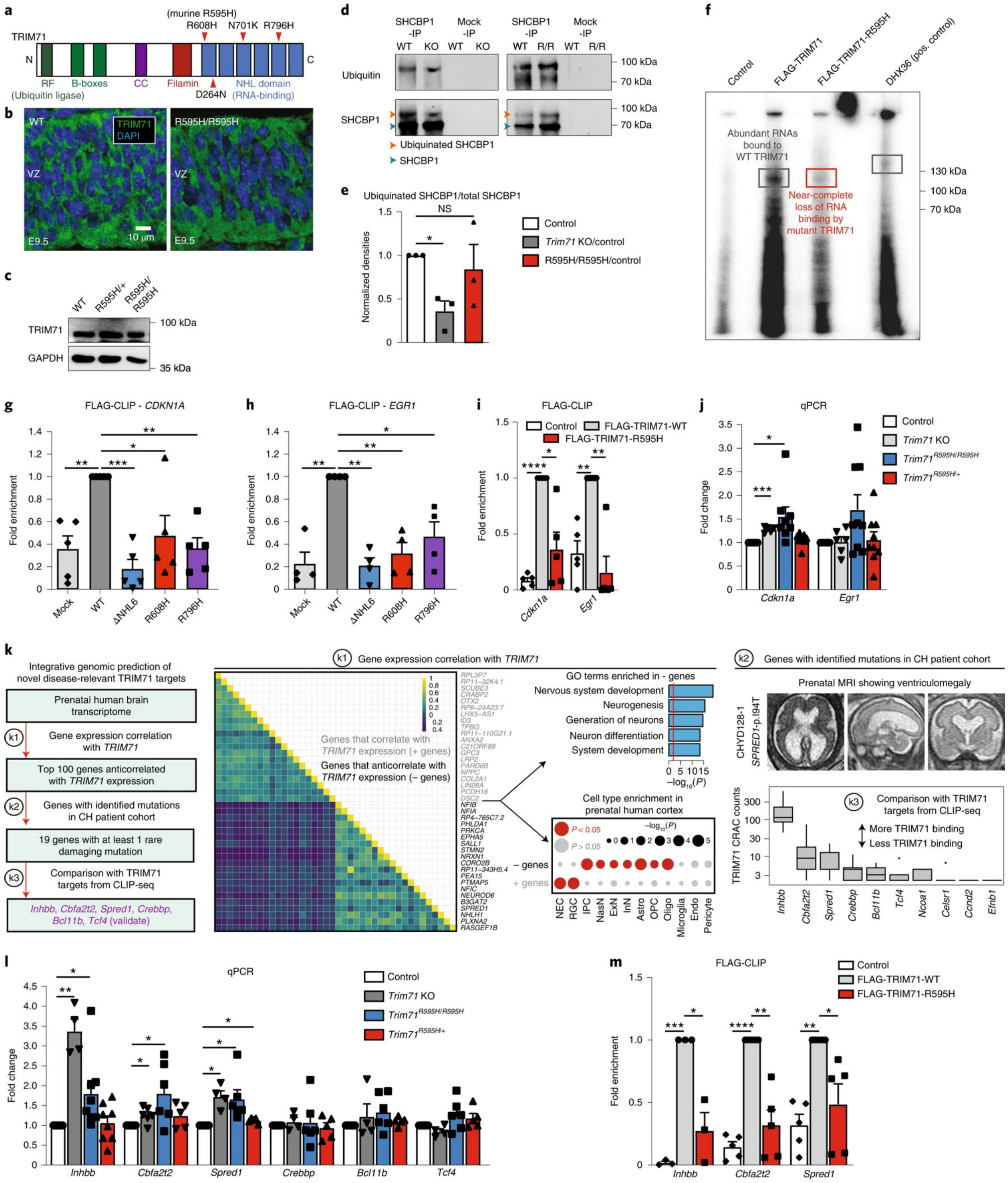

Fig. 7 |. CH mutations impair TRIM71 binding to its RNA targets, including the novel target *Spred1*.

a, The TRIM71 polypeptide domain schematic shows clustering of all mutations in the RNA-binding NHL domain. **b**, TRIM71 immunostaining in the E9.5 forebrain neuroepithelia of WT and *Trim71*$^{R595H/R595H}$. **c**, TRIM71 immunoblot in WT, *Trim71*$^{R595H/+}$ and *Trim71*$^{R595H/R595H}$ mESCs. **d**, Immunoblots showing ubiquitin and SHCBP1 signals of SHCBP1-IP from *Trim71*$^{fl/fl}$, *Trim71*-KO, WT and *Trim71*$^{R595H/R595H}$ mESCs differentiated with RA. SHCBP1 showed two bands; the upper band coincides with the ubiquitin signal. **e**, Quantitation of the SHCBP1 bands from SHCBP1-IP. Top SHCBP1 was normalized to total immunoprecipitated SHCBP1 (top + bottom bands). *Trim71* KO and *Trim71*$^{R595H/R595H}$ values were then normalized to their respective controls. **f**, Autoradiograph of PAR-CLIP samples from control (negative), FLAG-TRIM71-WT, FLAG-TRIM71-R595H and DHX36 (positive control) showing protein-bound RNA. Boxes indicate expected size of TRIM71 protein or DHX36 protein. **g–i**, CLIP-qRT–PCR enrichment of *CDKN1A* or *EGR1* upon co-precipitation with Flag-Ctrl and human Flag-TRIM71-WT, −ΔNHL6, −R608H and -R796H in HEK293T cells (**g**, **h**) or with endogenous mESC FLAG-TRIM71 and FLAG-TRIM71-R595H (**I**). Precipitated mRNA levels were normalized to input and to enrichment of housekeeping. **j**, qRT–PCR showing *Cdkn1a* and *Egr1* levels of mutant mESCs relative to respective controls. **k**, Stepwise approach to identify novel RNA targets of TRIM71. Significance was calculated by two-sided Fisher's exact test (GO analysis) or hypergeometric test (cell type enrichment analysis). Box plot (in **k3**): median (line) and 25th and 75th percentiles (box); whiskers extend up to 1.5 times the interquartile range from the top (bottom) of the box to the furthest datum within that distance, with outliers plotted as individual points. Analyzed datasets from ref. [12] and ref. [47]. For detailed statistical information (**k3**), see Supplementary Table 13. **l**, qRT–PCR of the six predicted TRIM71 targets from **k** of mutant mESCs relative to respective controls. **m**, CLIP-qRT–PCR enrichment of *Inhbb*, *Cbfa2t2* and *Spred1* upon co-precipitation with endogenous FLAG-TRIM71-WT and FLAG-TRIM71-R595H. Precipitated mRNA levels were normalized to input and to enrichment of housekeeping. Statistical significance was tested by one-sample *t*-test (**e**, **g–j**, **l**, **m**): $^{*}P < 0.05$, $^{**}P < 0.01$, $^{***}P < 0.001$, $^{****}P < 0.0001$ and NS (not significant): $P > 0.05$. Data are represented as mean ± s.e.m., overlaid with individual data points. For detailed statistical information (**e**, **g–j**, **l**, **m**), see Supplementary Table 13. Source data are provided.

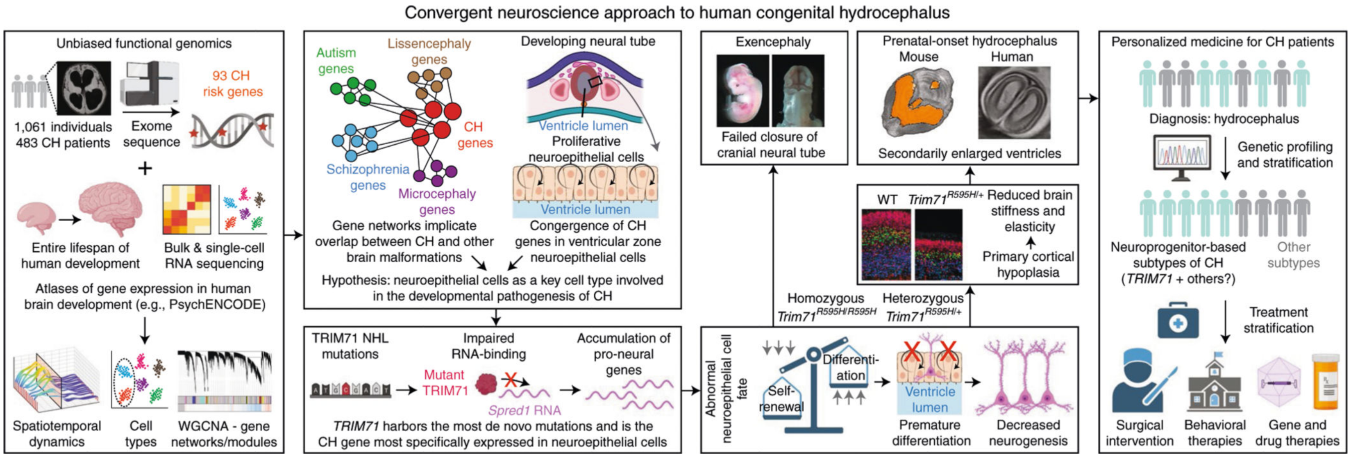

Fig. 8 |. Graphical summary of findings.

Integrative genomics combining exome sequencing data from the largest international cohort of human patients with CH to date with large-scale transcriptomic atlases of the developing human brain identified neuroepithelial cells lining the embryonic brain ventricles as a point of disease convergence. *TRIM71* harbors the most DNMs and is the CH risk gene most specifically expressed in neuroepithelial cells. CH-associated mutations in TRIM71 impair RNA binding and subsequent degradation, which lead to the accumulation of pro-neural differentiation signals. The combination of reduced proliferation and premature neuronal differentiation depletes the available neuroprogenitor pool. This results in neural tube closure defects and embryonic lethality of homozygous mouse mutants. Heterozygous mutations in either human or mouse result in a thinned cortical wall marked by reduced stiffness and elasticity, which facilitates secondary ventricular dilation and prenatal-onset hydrocephalus. Altogether, these findings suggest that some, or potentially many, forms of CH are, in fact, a congenital brain malformation with secondarily enlarged ventricles rather than a primary defect in CSF circulation. The identification of neuroprogenitor-based genetic subtypes of CH has major implications for clinical decision-making in the care of patients, such as the stratification of treatment strategies. In the long term, molecularly targeted gene therapies or pharmacological interventions may be developed to directly address the developmental pathology of CH.